



**HAL**  
open science

# Stress Perturbation From Aseismic Slip Drives The Seismic Front During Fluid Injection In A Permeable Fault

Nicolas Wynants-morel, Frédéric Cappa, Louis de Barros, Jean-paul Ampuero

► **To cite this version:**

Nicolas Wynants-morel, Frédéric Cappa, Louis de Barros, Jean-paul Ampuero. Stress Perturbation From Aseismic Slip Drives The Seismic Front During Fluid Injection In A Permeable Fault. *Journal of Geophysical Research: Solid Earth*, 2020, 10.1029/2019JB019179 . hal-02613516

**HAL Id: hal-02613516**

**<https://hal.science/hal-02613516>**

Submitted on 23 Jun 2022

**HAL** is a multi-disciplinary open access archive for the deposit and dissemination of scientific research documents, whether they are published or not. The documents may come from teaching and research institutions in France or abroad, or from public or private research centers.

L'archive ouverte pluridisciplinaire **HAL**, est destinée au dépôt et à la diffusion de documents scientifiques de niveau recherche, publiés ou non, émanant des établissements d'enseignement et de recherche français ou étrangers, des laboratoires publics ou privés.

Copyright

# JGR Solid Earth

## RESEARCH ARTICLE

10.1029/2019JB019179

### Key Points:

- 3-D hydromechanical models show that injection-induced seismicity along a permeable fault is not limited to the pressurized volume
- Seismicity follows the migration of the shear stress concentration near the aseismic slip front rather than the fluid pressure front
- Once the shear stress front outpaces the pressure front, the seismicity migration accelerates and cannot be explained by fluid diffusion

### Supporting Information:

- Supporting Information S1
- Movie S1

### Correspondence to:

N. Wynants-Morel,  
 wynants@geoazur.unice.fr

### Citation:

Wynants-Morel, N., Cappa, F., De Barros, L., & Ampuero, J.-P. (2020). Stress perturbation from aseismic slip drives the seismic front during fluid injection in a permeable fault. *Journal of Geophysical Research: Solid Earth*, 125, e2019JB019179. <https://doi.org/10.1029/2019JB019179>

Received 3 DEC 2019

Accepted 8 MAY 2020

Accepted article online 19 MAY 2020

## Stress Perturbation From Aseismic Slip Drives the Seismic Front During Fluid Injection in a Permeable Fault

Nicolas Wynants-Morel<sup>1</sup> , Frédéric Cappa<sup>1,2</sup> , Louis De Barros<sup>1</sup> ,  
 and Jean-Paul Ampuero<sup>1</sup> 

<sup>1</sup>Université Côte d'Azur, CNRS, Observatoire de la Côte d'Azur, IRD, Géoazur, Sophia Antipolis, France, <sup>2</sup>Institut Universitaire de France, Paris, France

**Abstract** Fluid pressure changes affect fault stability and can promote the initiation of earthquakes and aseismic slip. However, the relationship between seismic and aseismic fault slip during fluid injection remains poorly understood. Here, we investigate, through 3-D hydromechanical modeling, the spatiotemporal evolution of seismicity and aseismic slip on a permeable, slip-weakening fault subjected to a local injection of fluid, under different prestress conditions. The model results in an expanding aseismic slip region, which concentrates shear stress at its edge and triggers seismicity. The aseismic slip dominates the slip budget, whatever the initial fault stress. We find that the seismicity is collocated with the aseismic rupture front rather than with the fluid pressure diffusion front. On faults initially far from failure, the aseismic rupture front is located behind or at the pressure front. On faults initially closer to failure, the model predicts that both the rupture front and the seismicity outpace the pressurized zone, resulting in a sharp increase of the migration velocity and released moment of the seismicity. Insights gained from this modeling study exhibit various features that are observed in sequences of induced earthquakes in both field experiments and natural reservoir systems and can help guide the interpretation of past and future observations of induced seismicity.

**Plain Language Summary** The injection of fluids deep below ground can induce earthquakes, but it can also trigger slow deformations. Studying the relationship between fluid perturbation and seismic and aseismic deformations is fundamental to understand the mechanisms of injection-induced seismicity in order to mitigate seismic risk. Here, we present results of computer models of the response of a fault to fluid injection. We show that, in the presence of induced aseismic slip, the seismicity is not directly induced by the elevated fluid pressure but by the stresses generated by the expansion of the aseismic slip region. The seismicity initiates and diffuses along the edge of the stress-increase zone, rather than along the edge of the zone of elevated fluid pressure. We find two different behaviors depending on how stressed the fault is before injection. For a fault initially far from failure, the aseismic slip and the seismicity are confined in the pressurized zone. On the contrary, if a fault is initially close to failure, both the aseismic slip front and the seismicity front accelerate and outpace the fluid pressure front. Thus, the transient stress-increase associated with the aseismic slip and the initial stress conditions are key factors that control the triggering of seismicity.

## 1. Introduction

Fluid pressure changes affect fault stability and can promote the initiation of earthquakes. It has been widely documented that the injection or extraction of fluid in the first kilometers of underground rocks can generate seismicity in the contexts of oil and gas reservoirs, geothermal energy, and geological carbon sequestration (Ellsworth, 2013; Keranen & Weingarten, 2018). In recent years, there has been a rapid increase in the rate of induced seismicity in areas of active fluid injections, including relatively large induced earthquakes like the 2011  $M_w$  5.7 and 5.0 earthquakes near Prague in Oklahoma, United States (Keranen et al., 2013), the  $M_w$  5.8 Pawnee, Oklahoma, in 2016 (Yeck et al., 2017), or the 2017  $M_w$  5.5 earthquake near an enhanced geothermal site in Pohang, South Korea (Grigoli et al., 2018; Kim et al., 2018; Lee et al., 2019). Although induced earthquakes are predominantly associated with wastewater disposal, gas production can also induce earthquakes with moment magnitudes up to 3.6 (2012) and 3.4 (2017) in the Groningen field in the Netherlands (Candela et al., 2019; van Thienen-Visser & Breunese, 2015), as well as hydraulic fracturing

with moment magnitudes ranging from 2 to 4.6 (Clarke et al., 2014; Holland, 2013; Schultz et al., 2015), including the 2015  $M_w$  3.9 earthquake in western Canada (Bao & Eaton, 2016). These induced earthquakes are a growing concern and a hazard that needs to be controlled in order to develop a safer and cleaner energy future. Thus, it is important to understand how fluid pressure changes can modify subsurface stresses and trigger an earthquake.

While industrial fluid manipulations can generate earthquakes, this is not systematic. Fluids can also induce aseismic deformations associated with a slow rupture propagation without any detectable seismic event. Indeed, a large aseismic region surrounding the injection zone has been observed both at the reservoir scale (Cornet, 2012, 2016; Cornet et al., 1997; Hopp et al., 2019; Lengliné et al., 2017; Wei et al., 2015; Zoback et al., 2012) and during in situ experiments at the decametric scale (De Barros et al., 2016; Duboeuf et al., 2017; Guglielmi et al., 2015). In these small-scale experiments, it has been shown that most (>95%) of the deformation induced by fluid injection is aseismic (De Barros et al., 2016, 2018, 2019; Duboeuf et al., 2017; Goodfellow et al., 2015).

In the framework of injection-induced earthquakes, the conventional conceptual model corresponds to fault reactivation by an increase in fluid pressure that reduces the effective normal stress on the fault and brings the fault strength closer to the Coulomb failure criterion (Hubbert & Rubey, 1959). Later, this model was improved by including poroelastic stress changes within the pressurized volume and in the surrounding rock mass (Segall, 1989) and earthquake nucleation effects (Segall & Lu, 2015). The model shows that, at large distances from the injection, poroelastic stresses dominate over the fluid pressure increase (Goebel et al., 2017). Recently, based on field experiments and numerical simulations, Bhattacharya and Viesca (2019), Cappa et al. (2018, 2019), De Barros et al. (2016, 2018), and Guglielmi et al. (2015) have proposed a model of injection-induced aseismic slip which transmits an elastic stress perturbation that triggers seismicity beyond the fluid-pressurized zone. The important role of aseismic slip was recently confirmed in hydraulic fracturing-induced seismicity at the kilometer-scale in a deep reservoir (Eyre et al., 2019), and in a comparison of injection-induced earthquakes in in situ experiments and in the Central United States (Huang et al., 2019). Some studies have concluded that stress transfer between seismic events (i.e., earthquake interactions) can also play a significant role during a sequence of induced seismicity (Catali et al., 2016; Schoenball & Ellsworth, 2017). Models of multiple brittle asperities embedded in creeping faults indicate that earthquake interactions are dominantly driven by aseismic slip, rather than by direct static stress transfer between earthquakes (Dublanche, 2019a; Lui & Lapusta, 2016; Luo & Ampuero, 2017). Thus, among the potential triggering mechanisms of induced seismicity, fluid pressure change is likely more prominent at small distances around the injection, whereas poroelastic stress changes and stress perturbation through aseismic slip or earthquake interactions may outpace the fluid pressure migration at large distances.

However, although hydraulic processes and elastic stress interactions are considered to be efficient triggers of seismicity, the main mechanisms and controlling parameters of injection-induced seismicity remain unclear. Thus, it is crucial to identify the relative contributions of the fluid pressure diffusion and stress perturbation on fault rupture during fluid injection because (1) some models relate the growth of the seismicity cloud only to the diffusion of elevated fluid pressure activating critically stressed faults (Shapiro et al., 1997; Shapiro et al., 2002) and (2) other models relating the potential magnitude of induced earthquakes and injection parameters assume that the rupture is fully seismic and remains confined in the fluid pressurized zone (McGarr, 2014; Shapiro et al., 2011). Thus, these models do not consider the rupture modes (i.e., seismic versus aseismic slip) nor the stress perturbation and rupture propagation outside the pressurized zone, although seismicity has been observed outside this zone (Eyre et al., 2019; Goebel et al., 2016; Megies & Wassermann, 2014; Stark & Davis, 1996).

Consequently, once the initial fault activation occurs during fluid injection, the process surrounding the triggering and migration of seismicity is uncertain, and this may have a significant impact on the interpretation of the spatiotemporal evolution of seismicity and on the design of mitigation and monitoring strategies. Therefore, here we address the following key question: Are the seismicity triggering and migration processes directly linked to the fluid pressure diffusion or to others mechanisms?

In this study, we investigate the influence of the fluid pressure diffusion and the stress perturbation generated by the growing aseismic rupture in a permeable fault on the triggering of seismicity during a fluid injection using three-dimensional two-way-coupled hydromechanical modeling. A variety of numerical models

have been used to study the mechanisms of injection-induced faulting and the triggering of seismicity. While early studies focused on fault reactivation assuming a Coulomb failure criterion (Jaeger & Cook, 1984) with a constant friction coefficient (Aochi et al., 2014; Cappa & Rutqvist, 2011), recent studies include weakening and time-dependent characteristics of fault friction (i.e., slip-weakening or rate-and-state friction laws) to simulate fully dynamic rupture both for injection (Cappa & Rutqvist, 2012; Galis et al., 2017; Jin & Zoback, 2018a; Norbeck & Horne, 2016; Pampillón et al., 2018; Urpi et al., 2016) and production (Buijze et al., 2017, 2019). However, most models consider a two-dimensional geometry, and the coupled hydromechanical mechanisms are not completely considered. We assume a three-dimensional fault within an initial strike-slip stress regime. During the fluid injection, the hydraulic and frictional properties of the fault can change, which in turn may influence fault slip and opening, and the partitioning of seismic and aseismic ruptures. We consider an injection scenario where the flow rate increases quickly until a maximum value that is maintained constant over tens to hundreds of seconds. The injection occurs into a single hydromechanically homogeneous fault, governed by a slip-weakening friction law to simulate both seismic and aseismic slip, and by stress-dependent permeability changes to simulate fluid pressure diffusion. We analyze and discuss the distribution and evolution of the seismicity relative to the evolution of the fronts of fluid pressure and shear stress for different levels of fault “criticality” (initial fault stress relative to failure strength). Through our investigations, we show that the seismicity along a permeable fault is not limited to the pressurized zone and follows the migration of the shear stress front associated with the expansion of aseismic slip rather than the diffusion of the pressure front. Once the stress front outpaces the pressure front, the migration velocity of seismicity accelerates and cannot be explained by a classical time ( $t$ )—distance ( $r$ ) diffusion profile of the form  $r = \sqrt{Dt}$  where  $D$  is the hydraulic diffusivity. Finally, our study highlights the key role of the shear stress perturbation accompanying aseismic slip in the triggering and migration of earthquakes caused by fluid injection into a fault zone at reservoir depth.

## 2. Numerical Method, Model Setup, and Modeling Procedure

### 2.1. Model Setup: Geometry, Physical Properties, and Boundary Conditions

Our objective is to study the effect of a local fluid injection into a fault, at a typical reservoir depth of 3 km, on the generation and migration of seismic activity. We build a conceptual three-dimensional model (100 m  $\times$  45 m  $\times$  100 m) which considers fluid injection into a 70° dipping fault in a homogeneous elastic and impervious medium (Figure 1a).

The remote principal stresses ( $\sigma_{zz} = 81$  MPa,  $\sigma_{xx} = \sigma_{yy} = 70$  MPa) applied at the model boundaries and resolved on the fault planes are constant and follow the depth-gradient due to gravity ( $g = 9.81$  m/s<sup>2</sup>). We test different levels of fault proximity to failure by including a deviatoric component ( $\sigma_{xy} = 13.5$  to 18.5 MPa) to change the shear stress on the fault without modifying the normal stress among the tests. Before injection, we assume an initial fluid pressure ( $P_0$ ) of 30 MPa and a hydrostatic gradient with depth.

Injection is prescribed at a point source located at the center of the fault (Figure 1c). During injection, the volume of injected fluid per unit of time (i.e., flow rate) increases at a constant rate until a maximum value is reached, then is kept constant (Figure 2a). At the injection point, the fluid pressure on the fault increases gradually from an initial value of 30 MPa to a maximum value of 68.4 MPa (Figure 2b). We model a short-duration, high-rate injection in order to test an extreme and fast fluid pressurization relative to the initial state of effective stress on the fault at the injection point ( $\sigma_{no}' = 41.3$  MPa and  $\tau_o = 16.8$  MPa). The simulations are stopped when the ruptured area reaches 75% of the total fault area (i.e., before reaching the model boundaries). Therefore, the total time of injection is different from one simulation to another; it is 190 s in our reference case.

Hydromechanical and frictional properties of the fault and elastic properties for rocks are assumed uniform and set to typical values (Table 1). These properties are consistent with crustal reservoir conditions, for instance, in Oklahoma, a region of pronounced injection-induced seismicity (Barbour et al., 2017). The chosen values represent average values, except for the fault permeability which is initially high in this study ( $k \sim 10^{-9}$  m<sup>2</sup>) to explore the behavior of a highly conductive, intensively fractured fault zone that is representative of fast fluid conduits in subsurface reservoirs. Such values are consistent with in situ measurements with borehole hydraulic packer tests (Jeanne et al., 2012). Fault stiffness values are assumed uniform on

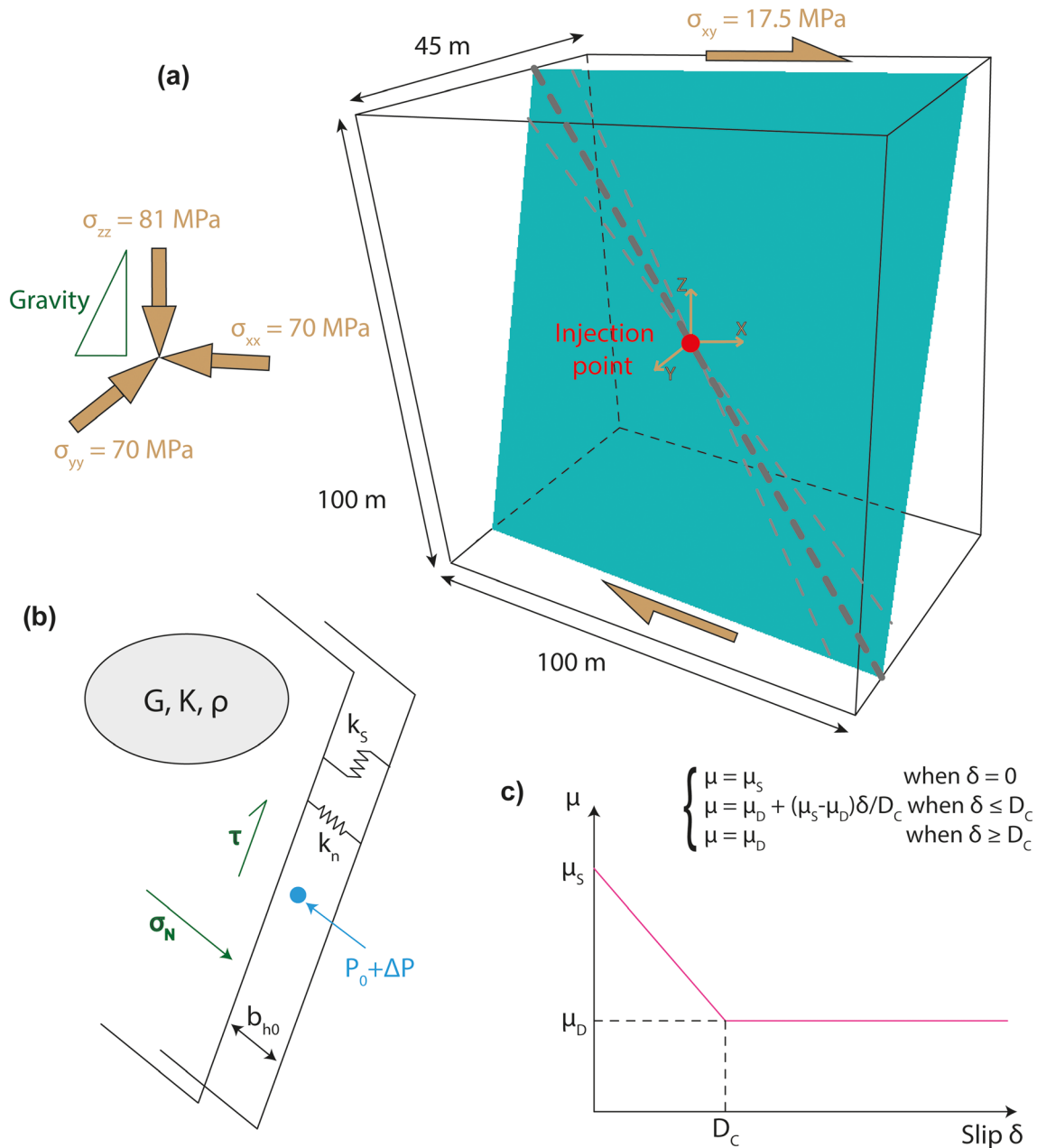


**Figure 1.** Model setup. (a) 3-D model geometry of the 70° dipping fault represented in light blue and the injection point in red at the center of the fault. The large brown dashed line intersecting the injection marks the position of a cross section used to measure profiles of fluid pressure and stress along the fault, the small dashed lines delimit a 10° zone around the cross section. The initial state of stress is represented with the vertical ( $\sigma_{zz}$ ) and horizontal ( $\sigma_{xx}$  and  $\sigma_{yy}$ ) stresses, and a deviatoric component ( $\sigma_{xy}$ ) for simulating a strike-slip stress regime. The gradient of stress with depth and gravity is indicated as a green triangle that gets larger downwards. (b) Schematic representation of the fault hydraulic and mechanical conditions, with the hydraulic aperture ( $b_{ho}$ ), the shear ( $k_s$ ) and normal ( $k_n$ ) stiffness, the rock shear ( $G$ ) and bulk ( $K$ ) modulus, the rock density ( $\rho$ ), the shear ( $\tau$ ) and normal stress ( $\sigma_n$ ) resolved on the fault, the fluid pressure ( $P_0$ ) and fluid overpressure ( $\Delta P$ ) caused by the fluid injection. (c) Linear slip-weakening friction with slip ( $\delta$ ), static friction coefficient ( $\mu_s$ ), dynamic friction coefficient ( $\mu_d$ ), and critical slip distance ( $D_c$ ).

the fault and correspond to typical values (e.g., Buijze et al., 2019). The values adopted in our simulations allow us to avoid overdamped slip velocity while keeping a reasonable computational cost.

A static friction coefficient of 0.6 is assumed, which is a typical value for faults at crustal conditions (Byerlee, 1978). Values for the dynamic friction coefficient ( $\mu_d$ ) and the critical slip distance ( $D_c$ ) can vary over a broad range (Marone, 1998; Rubino et al., 2017). For our reference case, we assume  $\mu_d$  of 0.4 and a

## SCU = 68%

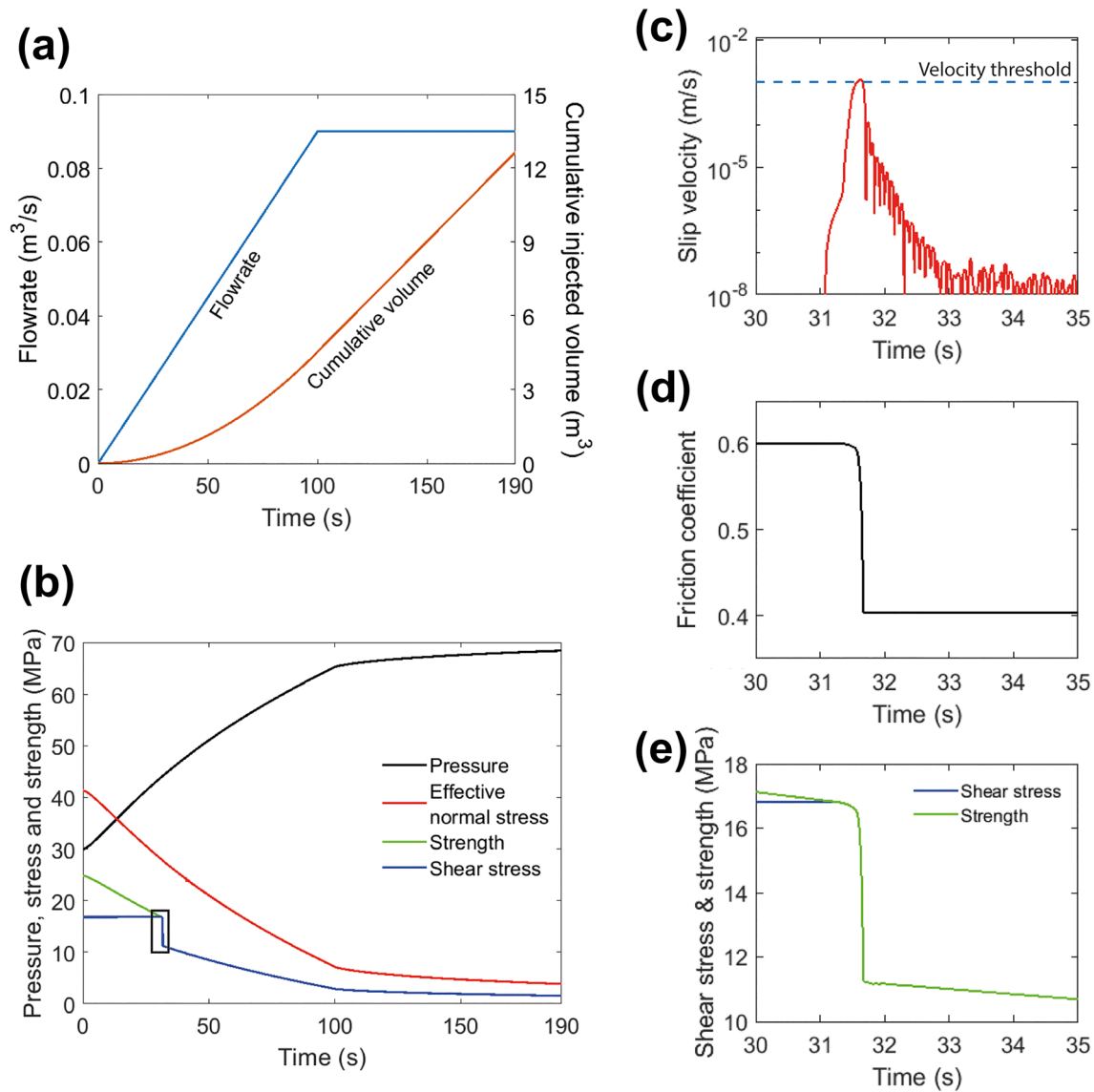


**Figure 2.** Injection procedure and fault response at injection. (a) Cumulative injected fluid volume and flowrate as a function of time. (b) Changes in fluid pressure (black), effective normal stress (red), shear stress (blue), and shear strength (red) as a function of time at the injection point. Close-up view of (c) the slip velocity, (d) the friction coefficient, (e) the shear strength (green), and stress (blue) during a seismic event. The blue horizontal dashed line in panel (c) represents the threshold of slip velocity (1 mm/s) to detect the transition between aseismic and seismic slip.

$D_c$  of 10  $\mu\text{m}$  (Table 1). With these frictional parameters, upon fault reactivation, an abrupt frictional weakening can occur (Figures 2d and 2e). Usually, a fault heals over time; that is, the strength is progressively recovered (Marone, 1998), but the healing process is not well known during fluid injection. As the injection time is here very short, we assume that no healing occurred; that is, no recovery of the friction coefficient to its static value is considered and the fault can continue slipping slowly or slip intermittently, without further weakening, after its first seismic rupture.

The modeling procedure consists of two stages: (1) initialization of a static state-of-stress and fluid pressure field and (2) simulation of a fluid injection. We use an adaptive time stepping scheme depending on the unbalanced force ratio: If it gets higher than a defined range of values (that is if the force equilibrium on the fault is far from being reached), the time step decreases; if it gets smaller, the time step increases. It

**Table 1**  
*Model Parameters for the Reference Case*

Material properties	Model parameters	value of each parameter
Rock mechanical properties	Shear modulus ( $G$ )	15 GPa
	Bulk modulus ( $K$ )	25 GPa
	Density ( $\rho$ )	2,750 kg/m <sup>3</sup>
Elastic stiffness of the fault	Normal stiffness ( $k_n$ )	300 GPa/m
	Shear stiffness ( $k_s$ )	300 GPa/m
Slip-weakening frictional properties of the fault	Static friction ( $\mu_s$ )	0.6
	Dynamic friction ( $\mu_d$ )	0.4
	Critical slip distance ( $D_c$ )	10 $\mu$ m
Hydraulic properties of the fault	Initial aperture ( $bh_0$ )	200 $\mu$ m
	Initial fluid pressure ( $P_0$ )	30 MPa
	Dilation angle ( $\psi$ )	0° to 1°
Fluid properties	Fluid bulk modulus ( $K_w$ )	2 GPa
	Fluid density ( $\rho_w$ )	1,000 kg/m <sup>3</sup>
	Fluid viscosity ( $\mu_f$ )	10 <sup>-3</sup> Pa s
Stress state	Initial effective normal stress ( $\sigma_{no}'$ )	41.3 MPa
	Initial shear stress ( $\tau_0$ )	16.8 MPa
	Initial criticality ( $SCU = \tau_0/\mu_s\sigma_{no}'$ )	68%

allows us to model the interseismic periods with a relatively large time step (around 1 s) and the coseismic ruptures with a reduced time step comprised between 10<sup>-6</sup> and 10<sup>-3</sup> s. The simulation of the seismic ruptures is thus quasi-dynamic.

In a simulation, the evolution of fluid pressure, fault opening, fault slip, stress, friction, and hydraulic aperture are calculated. The evolution of the fluid pressure and stress fronts are also monitored. At the end of a simulation, the location, timing, and moment magnitude of seismic events are estimated using the criteria defined in section 2.4.

## 2.2. Inherently Discrete Rupture Model

A three-dimensional (3-D) hydromechanical model of a fluid injection in a single permeable, slip-weakening fault is developed for this study using a 3-D Distinct Element Code (3DEC, Itasca Consulting Group, Inc., 2016). We consider a two way-coupled hydromechanical model including discrete ruptures for the generation of seismicity. Our earthquake rupture model falls into the class of “inherently discrete models” (Rice, 1993). We use a slip-weakening friction model with a short critical slip distance ( $D_c$ ) leading to a very small characteristic length scale for nucleation (Ben-Zion, 2008; Rice, 1993). Given the values used in our simulations, the nucleation length varies between 0.02 and 0.05 m depending on the effective normal stress observed at rupture (Uenishi & Rice, 2003). The fault is divided in triangular cells whose size (0.7 m) is larger than the earthquake nucleation size, thus each cell can be triggered independently from the others (Ben-Zion & Rice, 1993). This stays valid even for large fluid pressure and thus small effective normal stress. Moreover, the stability of the fault is verified using the critical stiffness  $K_C$  of the fault, which varies between 320 and 820 GPa/m with the fluid pressure observed at rupture (e.g., Ampuero et al., 2002). As the stiffness  $K$  of a single cell of the fault is equal to 28 GPa in our model, the criterion for single-cell instability,  $K < K_C$ , is verified for all values of pressure observed at rupture in our simulations. This setting represents, approximately, heterogeneous quasi-independent fault segments (Rice, 1993). This class of models was previously used for modeling injection-induced seismicity (Baisch et al., 2010; McClure & Horne, 2010), and tends to generate a large number of small seismic events. However, comparisons between inherently discrete and continuum models have shown that results are qualitatively similar for short-duration, high-rate injection (McClure & Horne, 2010, 2011). Inherently discrete models can reproduce complex seismic sequences on a single fault with realistic seismological features compatible with observations, such as a Gutenberg-Richter frequency-magnitude distribution of events (Ben-Zion & Rice, 1993, 1995; Carlson & Langer, 1989a), foreshocks (Rice, 1993), aftershocks following an Omori law (Ziv & Rubin, 2003), repeating earthquakes (Rice & Ben-Zion, 1996), creep events (Carlson & Langer, 1989b), and episodic tremor and slow slip (Ben-Zion, 2012).

### 2.3. Distinct Element Method

The Distinct Element Method (DEM) (Cundall, 1988) used in the 3DEC code (Itasca Consulting Group, Inc., 2016) is a numerical technique for simulating discontinuous media that consist of an assemblage of discrete blocks (i.e., rock) and discontinuities (i.e., faults, fractures, joints). Each individual block is discretized into an internal finite difference mesh consisting of tetrahedral zones and nodes, while the discontinuities are treated as distinct boundary conditions between blocks. The method uses an explicit time-marching procedure. During each time step of the simulation, the method uses force-displacement relations describing the interaction between blocks. The positions of blocks are updated through the differential equations of motion (Newton's laws) and constitutive equations to calculate the velocity, displacement and nodal forces at each time step, and determine block translation and rotation. The discontinuity forces are then updated based on constitutive laws. Thus, the code can simulate the coupling between stress and fluid flow in discrete faults embedded in impervious or permeable deformable rocks. The hydraulic aperture and permeability of a discontinuity (Figure 1b) are affected by the mechanical deformation, while the fluid pressure affects the mechanical computation at each time step.

In this study, we use this approach to calculate the fluid pressure, the fault displacement, and stress. The method has been previously used to evaluate the hydromechanical behavior of fault zones during fluid injection (Cappa et al., 2018; Guglielmi et al., 2008). Additionally, we here estimate earthquake source properties using seismological assumptions.

### 2.4. Fluid Flow and Hydromechanical Coupling

Injection of fluid leads to changes of pressure and fluid flow in a fault, and consequently, changes of stress over the fault surface and changes in aperture follow. The cubic law (Witherspoon et al., 1980) governs the fluid flow in the fault:

$$\vec{Q} = -\frac{b_h^3 \cdot w}{12\mu_f} \nabla P \quad (1)$$

where  $\vec{Q}$  is the flow rate vector ( $\text{m}^3/\text{s}$ ),  $\nabla P$  is the fluid pressure gradient ( $\text{Pa}/\text{m}$ ),  $\mu_f$  is the viscosity of fluid ( $\text{Pa s}$ ),  $w$  is the fault width ( $\text{m}$ ), and  $b_h$  is the hydraulic aperture ( $\text{m}$ ), which is defined as

$$b_h = b_{ho} - \frac{\Delta\sigma'_n}{k_n} + \Delta u_s \cdot \tan\psi \quad (2)$$

where  $b_{ho}$  ( $\text{m}$ ) is the initial aperture at zero normal stress,  $\Delta\sigma'_n$  is the increment in effective normal stress ( $\text{Pa}$ ),  $k_n$  is the normal stiffness ( $\text{Pa}/\text{m}$ ),  $\Delta u_s$  ( $\text{m}$ ) is the shear slip increment, and  $\psi$  is the dilation angle ( $^\circ$ ). Dilation occurs only as the fracture slips. The hydraulic aperture is linked to the permeability ( $\text{m}^2$ ) as follows (Jaeger & Cook, 1984):

$$k = \frac{b_h^2}{12} \quad (3)$$

Experimental and numerical analyses have shown that the cubic law is adequate to simulate fluid flow and hydromechanical effects along smooth surfaces (Brown, 1989; Zhang et al., 2019).

The numerical solution for fluid flow is based on a fluid network structure, discretized in nodes (Itasca Consulting Group, Inc., 2016). Each node has a uniform fluid pressure and can communicate with the neighboring nodes. Thus, the fluid flow is governed by the difference in pressure between adjacent nodes. At each time step ( $\Delta t$  in  $\text{s}$ ), the fluid pressure ( $P$  in  $\text{Pa}$ ) at each fluid node is updated considering the net fluid flow entering the node and the node volume change ( $\Delta V$ ):

$$P = P_0 + K_w Q \frac{\Delta t}{V} - K_w \frac{\Delta V}{V_m} \quad (4)$$

where  $P_0$  is the initial fluid pressure ( $\text{Pa}$ ) at the considered node,  $K_w$  ( $\text{Pa}$ ) is the fluid bulk modulus, and  $V_m = (V^t + V^{t-1})/2$  with  $V^{t-1}$  and  $V^t$ , the node volumes in the previous and new time steps ( $\text{m}^3$ ), respectively.

### 2.5. Fault Displacement and Slip-Weakening Friction

In DEM, normal ( $\Delta F_n$ ) and shear ( $\Delta F_s$ ) elastic force increments on the fault are calculated at each node of the mesh cells as follows:

$$\Delta F_n = -k_n \cdot \Delta u_n \cdot A_c \quad (5)$$

$$\Delta F_s = -k_s \cdot \Delta u_s \cdot A_c \quad (6)$$

where  $k_n$  and  $k_s$  are the normal and shear stiffnesses (Pa/m) (Figure 1b),  $\Delta u_n$  and  $\Delta u_s$  are the normal and shear displacement increments (m), and  $A_c$  is the contact area (m<sup>2</sup>), corresponding to the area of a mesh cell. The calculated shear force ( $F_s$ ) is compared to the shear strength ( $F_s^\mu$ ) of the Mohr-Coulomb failure criterion (Jaeger & Cook, 1984):

$$F_s^\mu = \mu \cdot F_n + c \cdot A_c \quad (7)$$

where  $\mu$  is the coefficient of friction and  $c$  is the cohesive strength (Pa). This is more commonly expressed through the following constitutive equation:

$$\tau_f = c + \mu(\sigma_n - p) = c + \mu\sigma_n' \quad (8)$$

where  $\tau_f$  is the shear strength of the fault (Pa),  $\sigma_n$  is the normal stress (Pa), and  $p$  is the fluid pressure (Pa) acting on the fault. The increase in fluid pressure in the fault induces a reduction in the effective normal stress ( $\sigma_n' = \sigma_n - p$ ). When the fluid pressure reaches a critical value that satisfies the Coulomb failure criterion, the fault is reactivated, slip is initiated and the slip velocity increases. The cohesive strength is set null in this study. During slip, the shear force is maintained equal to the shear strength and the coefficient of friction evolves as a function of the shear slip. We use the linear slip-weakening formulation (Ida, 1972) to describe this evolution of friction. The law assumes that the friction coefficient depends on the amount of slip ( $\delta$ ) and decays linearly from a peak static value ( $\mu_s$ ) to a residual dynamic value ( $\mu_d$ ) over a critical slip distance ( $D_c$ ) (Figure 1c and Table 1). The slip can be either aseismic or seismic, depending on the rate of friction weakening. During a seismic event, the stress drop is thus controlled by the evolution of friction and effective stress. This is different from modeling approaches that directly assign a value of stress drop (e.g., Baisch et al., 2010; Izadi & Elsworth, 2015).

### 2.6. Detection of Seismic Slip and Seismic Source Properties

A seismic catalog is extracted from the continuous monitoring of slip velocities calculated in each cell during the simulation using the following criteria to define a seismic event:

1. Slip on a cell is considered seismic if the slip velocity is equal or greater than a typical threshold of dynamic slip velocity ( $v_{\text{thres}}$ ) defined by the rock elastic properties and the fault frictional properties (Cochard & Madariaga, 1994):

$$v_{\text{thres}} = \frac{\sigma_n'(\mu_s - \mu_d)}{G} 2c_s \quad (9)$$

where  $c_s$  is the shear wave speed (m/s) and  $G$  is the shear modulus (Pa). For injection-induced seismicity, typical values for this velocity threshold range from 0.1 mm/s to 0.1 m/s (Gischig, 2015; McClure, 2015; McClure & Horne, 2011). Here, we adopt a value of 1 mm/s.

2. We set a minimum rupture area as the area of a compact zone, physically connected, with at least  $N$  cells having a slip velocity equal or greater than  $v_{\text{thres}}$ . In this study, to consider a constant size for the smallest seismic events, the mesh size is uniform (0.7 m). Thus, the smallest event size is  $N \times 0.21 \text{ m}^2$ . We consider initially  $N = 1$ .
3. A seismic event ends when the slip velocity decreases below  $v_{\text{thres}}$  for all cells involved.

Thus, the algorithm measures the slip velocity in all cells to separate seismic and aseismic slip. The nearby cells considered over a seismic period are grouped in space to define the seismic rupture surface area. The

hypocenter is identified as the first cell whose slip velocity exceeds  $v_{\text{thres}}$ . The event size is quantified by the seismic moment ( $M_o$ ) and the moment magnitude ( $M_w$ ):

$$M_o = AG\bar{u}_s \quad (10)$$

$$M_w = \frac{2}{3} \log(M_o) - 6 \quad (11)$$

where  $A$  is the ruptured area ( $\text{m}^2$ ) and  $\bar{u}_s$  is the average slip on the ruptured area (m).

An aseismic moment is calculated by applying Equation 10 to aseismic slip. The seismic/aseismic partitioning is measured using the ratios of seismic to aseismic moment released during the injection.

## 2.7. Analysis of Modeling Results

In order to interpret the modeling results in the following sections, we define two parameters: (1) the “initial fault criticality” that measures the closeness of prestress to failure before injection, and (2) the “shear stress contribution” that estimates the stress necessary to reach rupture during the injection.

### 2.7.1. Initial Fault Criticality: Closeness to Failure

We define the initial closeness to failure of the fault using the Shear Capacity Utilization (SCU) parameter proposed in Buijze et al. (2019), the ratio between initial shear stress and initial strength on the fault:

$$SCU = \frac{\tau_0}{\tau_{f_0}} = \frac{\tau_0}{\mu_s(\sigma_{n_0} - P_0)} \quad (12)$$

This parameter is computed before the injection starts. A SCU of 1 indicates that the fault is at failure and can slip, seismically or aseismically.

### 2.7.2. Shear Stress Contribution

We want to estimate the amount of shear stress increase required to reach rupture at a given time ( $t$ ) and location ( $\bar{x}$ ) on the fault. For this purpose, a Coulomb Failure Function (e.g., Jin & Zoback, 2018b) is considered:

$$CFF(\bar{x}, t) = \tau(\bar{x}, t) - \mu(\sigma_n(\bar{x}, t) - P(\bar{x}, t)) \quad (13)$$

Failure is reached when  $CFF(\bar{x}, t)$  vanishes, either by increasing the shear stress ( $\tau$ ) or the pressure ( $P$ ). In order to estimate the contribution of the shear stress in the nucleation of each seismic event, we first quantify the shear stress increment that is sufficient to reach rupture starting from the initial shear stress and pressure state, that is, the shear stress that negates the initial value of the Coulomb Failure Function. Then, the Shear Stress Contribution (SSC) is quantified as

$$SSC = \frac{\Delta\tau(\bar{x})}{-CFF(\bar{x}, 0)} = \frac{\Delta\tau(\bar{x})}{\mu(\sigma_n(\bar{x}, 0) - P(\bar{x}, 0)) - \tau(\bar{x}, 0)} \quad (14)$$

where  $\Delta\tau(\bar{x})$  is the shear stress variation from the initial state at the location  $\bar{x}$ , when the Mohr-Coulomb criterion (Equation 8) is reached. A SSC of 0 indicates that the failure is caused by the fluid pressure changes, while a SSC of 1 indicates that the failure is driven by the shear stress perturbation.

## 3. Modeling Results

This section presents the modeling results of the spatiotemporal evolution of seismicity and aseismic slip induced by the injection for different levels of initial closeness to failure (SCU). The evolution of the fronts of fluid pressure and shear stress are presented and compared with the conventional analytical solution of the pressure diffusion in a homogeneous, isotropic porous medium.

### 3.1. Fault Response to Fluid Injection

First, we examine the impact of the fluid injection on the spatiotemporal distribution of the seismicity and aseismic slip for a reference case with a SCU of 68% (Table 1 and Figures 2 to 5). Fault reactivation starts at the injection point after 31.6 s of injection at a pressure of 44.1 MPa (Figure 2b), corresponding to an

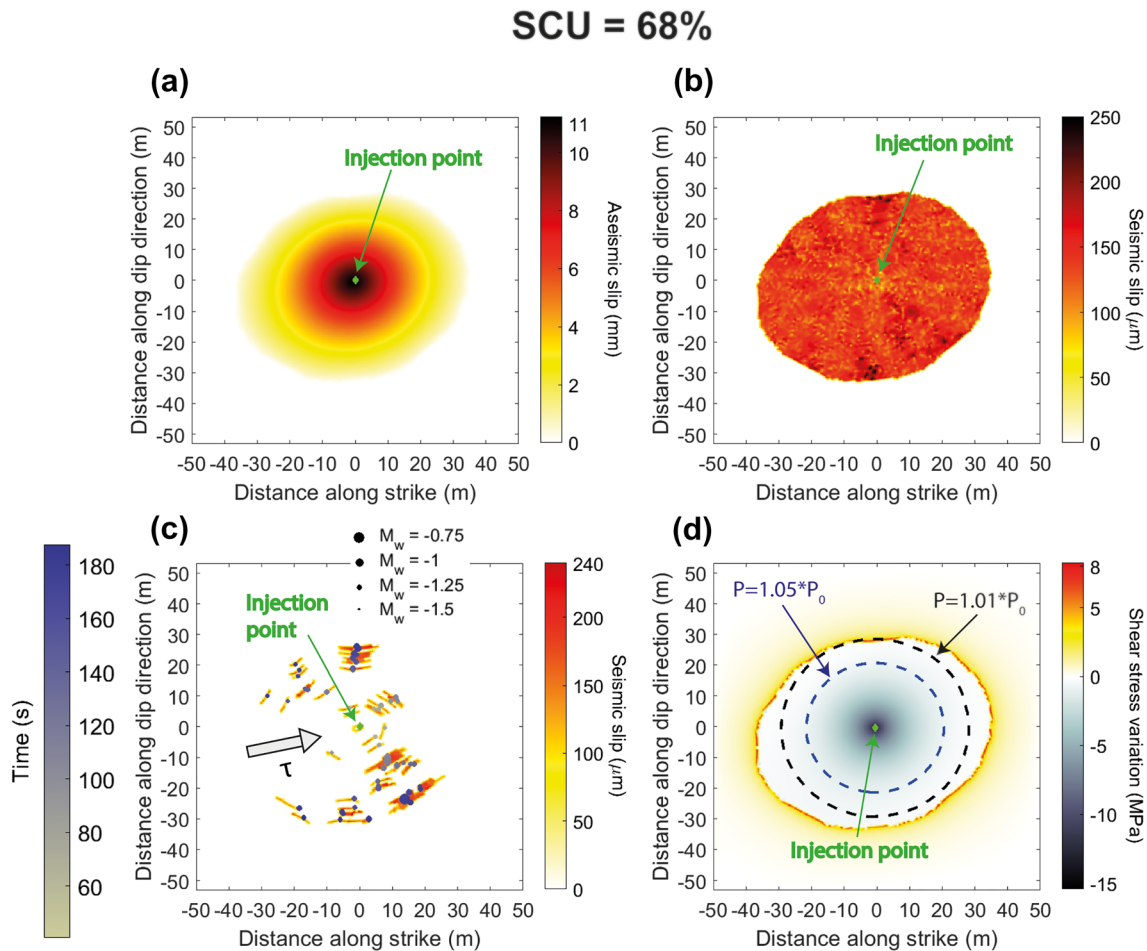


**Figure 3.** Snapshots of the spatial distribution of (a) aseismic and (b) seismic slip across the fault at the end of the injection. (c) Location and time of occurrence of seismic events with moment magnitude ( $M_w$ ) greater than  $-1.6$  together with the ruptured area and the amplitude of seismic slip for each individual event.  $\tau$  is the shear stress vector resolved on the fault plane. (d) Snapshot of shear stress changes at the end of injection relative to the initial state. The dashed black and blue circles represent the limit of the pressure front where increases in fluid pressure are 1% and 5% of the initial pressure before injection. In all panels, the injection point is represented by the green diamond at the center of the fault.

overpressure of 14.1 MPa relative to the initial state. As in this reference model, the effect of shear-induced dilation is not considered, the permeability depends only on effective stress and thus pressure diffusion is isotropic. The first rupture is a small seismic event at the injection point, with a stress drop of 5.6 MPa (Figure 2e) and a maximum slip velocity of 1.16 mm/s (Figure 2c). Afterward, fault slip develops and grows in size through a combination of aseismic slip and seismic events (see supporting information, Movie S1). A large aseismic slip patch (maximum length of 74 m and width of 59 m) develops with an asymmetric elliptical shape and an oblique orientation related to the initial strike-slip regime (Figure 3a). The slip area grows preferentially in the direction of shear stress vector resolved on the fault plane ( $\vec{\tau}$ ), which is also the direction of slip, consistent with the preferred elongation of static cracks in the mode II direction expected from fracture mechanics theory (e.g., Galis et al., 2017). The amplitude of the aseismic slip is maximum at the injection point (11.3 mm) and decays progressively toward the limits of the ruptured area (Figures 3a–3c). During reactivation, some fault elements slip seismically. The distribution of seismic slip is similar over the whole slipping area (Figure 3b). At the end of the test, seismic slip ranges from some microns to 0.249 mm, which is about 45 times smaller than the maximum aseismic slip, a small portion of the total deformation. As the seismic and aseismic slipping areas are identical at the end of injection, the released moment is mostly aseismic, with only 0.4% of seismic deformation on average.

We now consider only the events with a rupture area above  $1.5 \text{ m}^2$  (Figure 3c), which corresponds to a moment magnitude ( $M_w$ ) greater than  $-1.6$  and to a rupture area of at least 7 cells (see section 2.4 for

SCU = 68%

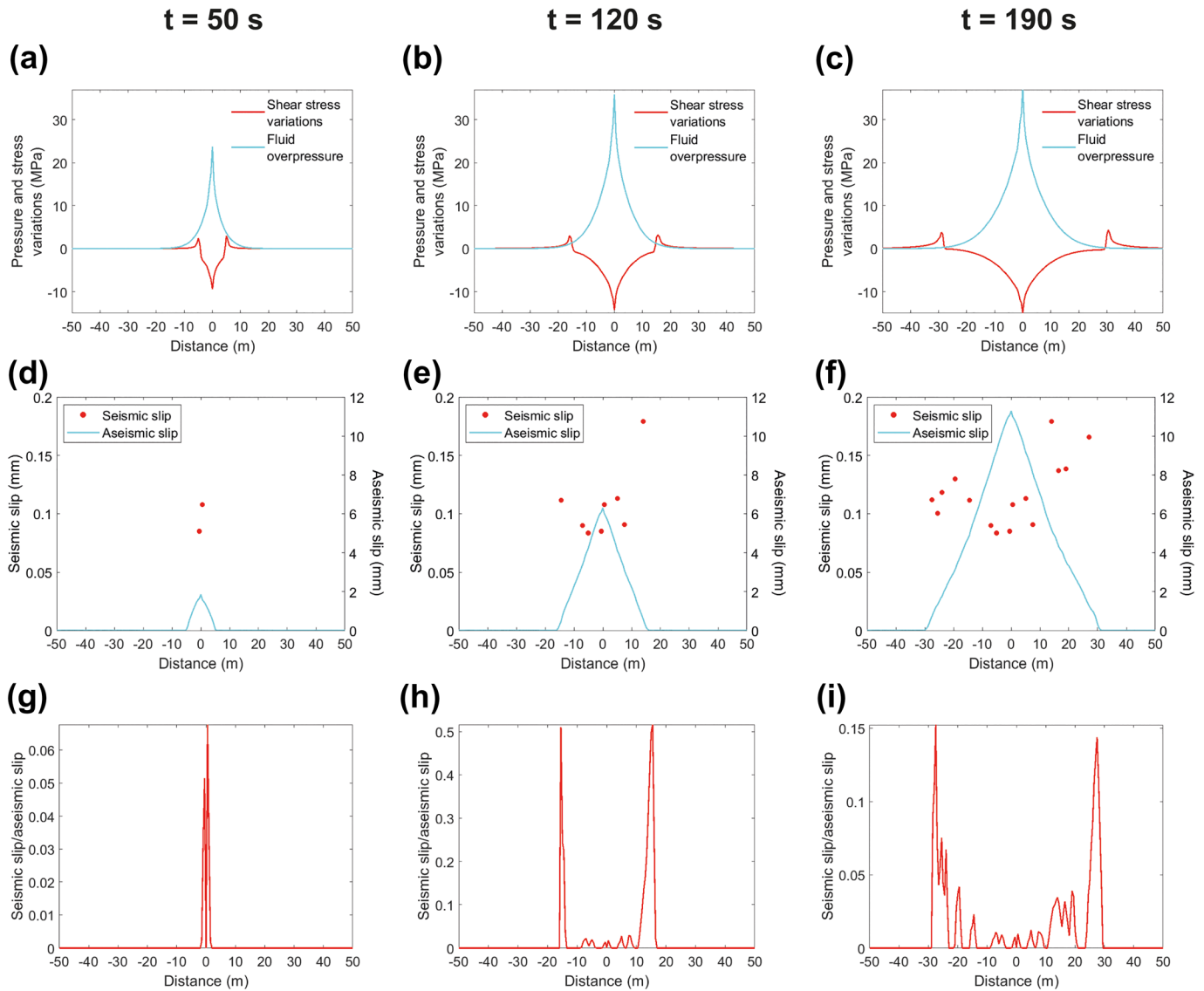


**Figure 4.** Profiles of (a–c) fluid pressure and shear stress changes, (d–f) aseismic slip (light blue) and peak seismic slip (red dots), and (g–i) the ratio of seismic to aseismic slip at three selected times, 50, 120, and 190 s. These profiles correspond to average values on a  $\pm 10^\circ$  area around the brown dashed line across the model geometry in Figure 1c.

details). This minimum magnitude is consistent with observations of induced earthquakes in recent reservoir-scale injection experiments (e.g. Kwiatek et al., 2019) in which only the largest events are detected, the smallest events being generally buried in the noise. This selection gives 55 distinct events, with magnitude ranging from  $-1.6$  to  $-0.7$ .

The seismic rupture areas are distributed heterogeneously on the fault (Figure 3c). Their hypocenters are mainly located perpendicular to the fault shear stress vector  $\vec{\tau}$  (i.e., along the minor axis of the slip ellipse), while almost no event occurred in the direction of the shear stress vector. The seismic patches are elongated in a direction locally parallel to the aseismic slip front (Figures 3c and 3d). The events are located on the edge of the zone of shear stress concentration near the rim of the overall slip area, along which the Coulomb Failure Function (CFF) is null at a given time. They are all triggered at the passage of the rupture front. There is no seismic event left around the injection point, which is consistent with seismological observations in highly instrumented decametric scale experiments (e.g., De Barros et al., 2018). The hypocentral distance

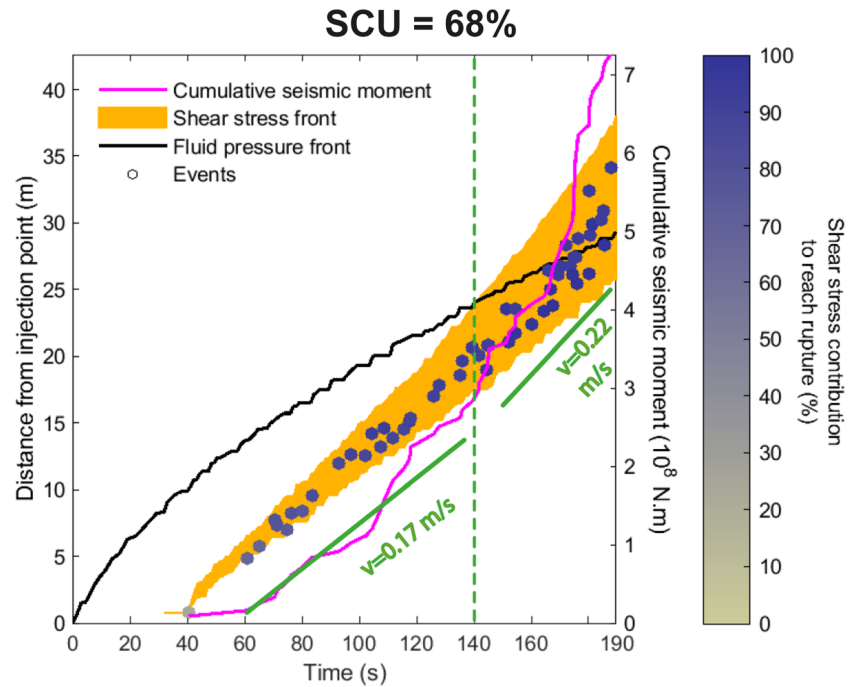


**Figure 5.** Time evolution of the distance of the seismicity (colored dots), the pressure front (black), and the shear stress front (orange zone) relative to the injection point. The cumulative seismic moment (purple) is also plotted as a function of time. The colorbar represents the shear stress contribution (defined in the section 2.7.2) to reach rupture for each seismic event. The vertical green dashed line marks the transition of the mean migration velocity of seismic events. The green straight line below seismicity indicates the mean migration velocity of events.

relative to the injection point and the magnitude of the events increase with time. Some events are located outside the pressurized zone, that is, outside the stimulation region (Figures 3c and 3d).

Aseismic and seismic slip have different spatial distributions. They are compared in Figures 4d–4f at three different times, 50, 120, and 190 s from the beginning of the injection. The simulation data are averaged on a zone covering an orientation of  $10^\circ$  around the oblique section represented by the gray dashed lines in Figure 1c, that is, close to the direction in which most of the seismicity occurred. The aseismic slip is maximal at the injection point and decays linearly with distance. Conversely, the seismic slip is smaller at the injection point and grows with distance. Consequently, the seismic-to-aseismic slip ratio increases with distance from the injection point. The maximum of this ratio is therefore always situated at the rupture front, while it reaches zero or small values around the injection point. As the spatial distribution of the seismic patches is discontinuous (Figure 3c), the seismic slip shows a heterogeneous distribution.

The aseismic slip (Figures 4d–4f) can be compared to the fluid pressure and stress changes (Figures 4a–4c). At all times, the shear stress drops within a large area around the injection point, which corresponds to the aseismic slip area and increases in the surrounding area (see also Figure 3d). The transition from negative to positive shear stress change corresponds to the rupture front, the outer rim of the aseismic front. Interestingly, at 50 s, the pressure perturbation is ahead of the rupture front, while at later times, the rupture front and associated shear stress perturbations outpace the pressure front. The pressure front can be defined as the contour where pressure is 1% or 5% greater than the initial pressure ( $P_0$ ). These two pressure contours are represented in Figure 3d at the end of the injection. The rupture front is located beyond the 5% overpressure front, and beyond the 1% overpressure front in the direction of  $\vec{\tau}$  and in the lower part of the fault. The aseismic rupture thus occurs at overpressure lower than 1.5 MPa, but induces pronounced shear stress perturbations with values up to 8 MPa. Therefore, the shear stress loading is likely the main triggering phenomenon of the rupture at times larger than 50 s.

To further understand the relationship between seismicity, aseismic deformation, pressure, and shear stress, we show in Figure 5 the seismicity in a distance-time diagram (so-called *R-T* plot, Shapiro et al., 1997),

together with the shear stress front and the fluid pressure front at 5% overpressure. We define the shear stress front as the locations with a shear stress equal or greater than 95% of the peak shear stress. As the rupture shape is elliptical (Figure 3d), the shear stress front forms a band that widens as the rupture ellipse grows with time. The seismicity always occurs on the shear stress front, and does not follow the pressure front. As the shear stress front starts to outpace the pressure front after 120 s (Figures 4b and 4c), the seismicity nucleates outside the stimulation zone, as observed after 165 s in Figure 5. The seismic events cannot be induced by the fluid overpressure after that time. In order to quantify the relative contribution of the fluid pressure and shear stress in the triggering of seismic events, we calculate the shear stress contribution required to induce failure (SSC, Equation 14). Close to the injection point, some events are partly induced by the pressure increase because SSC reaches 23% for the first event. Later in the injection, SSC varies between 50% and 99% for all other events (see supporting information, Figure S5). Therefore, shear stress loading dominates the seismic rupture initiation except for the first events initiated close to the injection point (Figure 5). The shear stress increase associated with the expansion of the aseismic slip is the dominant mechanism that triggers seismic events. Moreover, the shear stress contribution is more and more pronounced with increasing time and distance, as expected from Figure 4.

Two migration behaviors can be observed. Before 140 s, the rupture front and the seismicity front slowly expand with a mean velocity of about 0.17 m/s. After, the migration velocity of the rupture and seismicity fronts increases to a mean speed of 0.22 m/s. This transition occurs when the shear stress front starts to outpace the pressure front (Figures 4b and 4c). This acceleration of the seismicity migration is accompanied with a sharp increase of the seismic moment rate (Figure 5).

The possible effect of shear-induced dilation was investigated by changing the dilation angle to  $1^\circ$ , that is a typical value to ensure coupling between hydraulic aperture and fault slip (e.g., McClure & Horne, 2011) (see supporting information, Figures S1 and S2). Our model considers a two-way coupling, including the increased pressure causing stress changes and the permeability changes due to both effective stress and slip. Compared to the reference model (which ignores the effect of shear-induced dilation), the number of earthquakes and the seismic moment slightly decrease by about 2%. When the rupture front outpaces the pressure front, the acceleration of the seismicity front is less pronounced and decreased by 5%. For a similar rupture area, shear-induced dilation increases the final migration distance of the pressure front by 8%, but has a minor effect on the shear stress fronts and on the seismicity migration velocity which changes only of 0.01 m/s.

### 3.2. Effect of the Initial Fault Criticality

The initial closeness to failure of a fault is known to influence the slip and rupture extent (Ciardo & Lecampion, 2019; Gischig, 2015; Jin & Zoback, 2018b). Here, we study its impact on the spatiotemporal evolution of seismicity and aseismic slip. The initial closeness to failure is quantified by the initial Shear Capacity Utilization (SCU, Equation 12). Besides the reference case with a SCU of 68%, we examined four additional cases with SCU of 53%, 59%, 64%, and 71%, respectively. As in the reference case, these simulations have been stopped at a fixed rupture front threshold corresponding to 75% of the width of the fault. Moreover, only the events with a slipping patch over than  $1.5 \text{ m}^2$  are taken into account.

In all cases the seismicity front is delimited by the shear stress front and not by the fluid pressure front (Figure 6). However, two different behaviors are observed depending on the SCU value. For the cases with SCU = 53%, 59%, and 64%, the shear stress front remains behind the pressure front. The shear stress and pressure fronts slow down with distance and time. For the case with SCU = 71%, the shear stress front and the seismicity front show the two distinct phases previously described for the reference case (see section 3.1): they are first behind the pressure front, then they accelerate and outpace it. The cumulative seismic moment increases sharply during this accelerating migration phase. The distinction between the two behaviors can be related to the sign of the potential stress drop available through the initial stresses. If the stresses before injection are such that the shear stress is above the dynamic friction strength ( $\tau_o > \mu_d \sigma'_{no}$ ), the initial state has a positive contribution to stress drop ( $\tau_o - \mu_d \sigma'_{no}$ ), and thus provides additional potential energy to drive the slip front growth. This is the case when SCU = 68% and 71%. Otherwise, the potential stress drop given by the initial stresses is negative and resists against rupture. This is the case when SCU = 53%, 59%, and 64%.

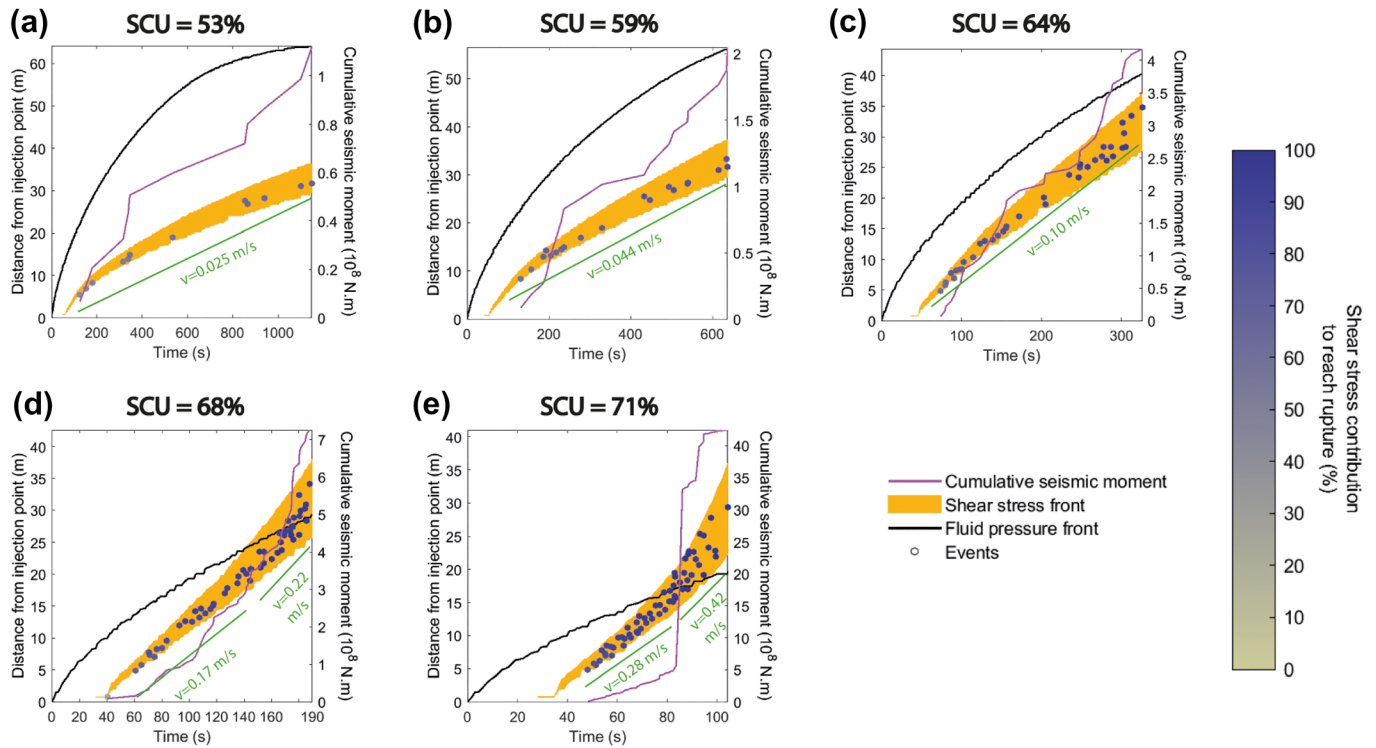


**Figure 6.** Parametric study on the initial fault criticality defined with SCU equals to (a) 53%, (b) 59%, (c) 64%, (d) 68%, and (e) 71%, respectively. Time evolution of the distance of the seismicity (colored dots), the pressure front (black), and the shear stress front (orange zone) relative to the injection point. The cumulative seismic moment (purple) is also plotted as a function of time. The colorbar represents the shear stress contribution (defined in the section 2.7.2) to reach rupture for each seismic event. The green straight line below seismicity indicates the mean migration velocity of events. Scales are different between panels.

When the rupture front is behind the pressure front, the mean migration velocity of seismicity also increases with the increase in SCU (0.025 to 0.28 m/s). In the second period for the high SCU case when the shear stress front starts to outpace the pressure front, the seismicity migration velocity increases from 0.22 to 0.42 m/s. Thus, the closer to failure is the fault initially, the faster is the seismicity migration.

Varying the initial closeness to failure affects the number and magnitude of the seismic events (Figures 7 and 8), and therefore the total seismic moment. The latter ranges from  $\sim 1.1 \times 10^8$  at SCU = 53% to  $\sim 46 \times 10^8$  N m at SCU = 71% (Figure 6). The closer to failure is the fault initially, the larger are the number and magnitude of seismic events. Indeed, 12, 19, 37, 55 and 61 seismic events nucleated from the lowest to the highest SCU, respectively. For small SCU, only small events ( $M_w < 0$ ) occur in the direction perpendicular to the fault shear stress vector  $\vec{\tau}$ . For large SCU, large events ( $M_w > 0$ ) occur, and cover a broader region around the injection point. Therefore, the seismic slip is more uniformly distributed around the injection point. As the rupture propagates faster with increasing SCU, the injection time is much smaller for large SCU simulations. Therefore, for a similar rupture surface, the maximal amplitude of the aseismic slip decreases with the increase of SCU, from 14 mm for a SCU of 53% to 7 mm for a SCU of 71% (Figures 7 and 8). Therefore, even if the deformation stays dominantly aseismic, the seismic-to-aseismic moment ratio increases with closeness to failure from 0.05% to 4% (Figure 9a). If the rupture is stopped for the same injected time and volume, the aseismic deformation is larger at the injection point for high SCU simulations (see supporting information, Figure S6). Given that larger SCU ruptures grow larger over the same injection interval, this is consistent with continuum models (e.g., Garagash & Germanovich, 2012).

The closeness to failure of a fault is also known to influence the shape of the induced rupture (Galis et al., 2019). Indeed, our models show that the shapes of the rupture patch evolve from nearly circular at low SCU to elongated ellipses at high SCU. The elongation of the rupture area occurs preferentially in the

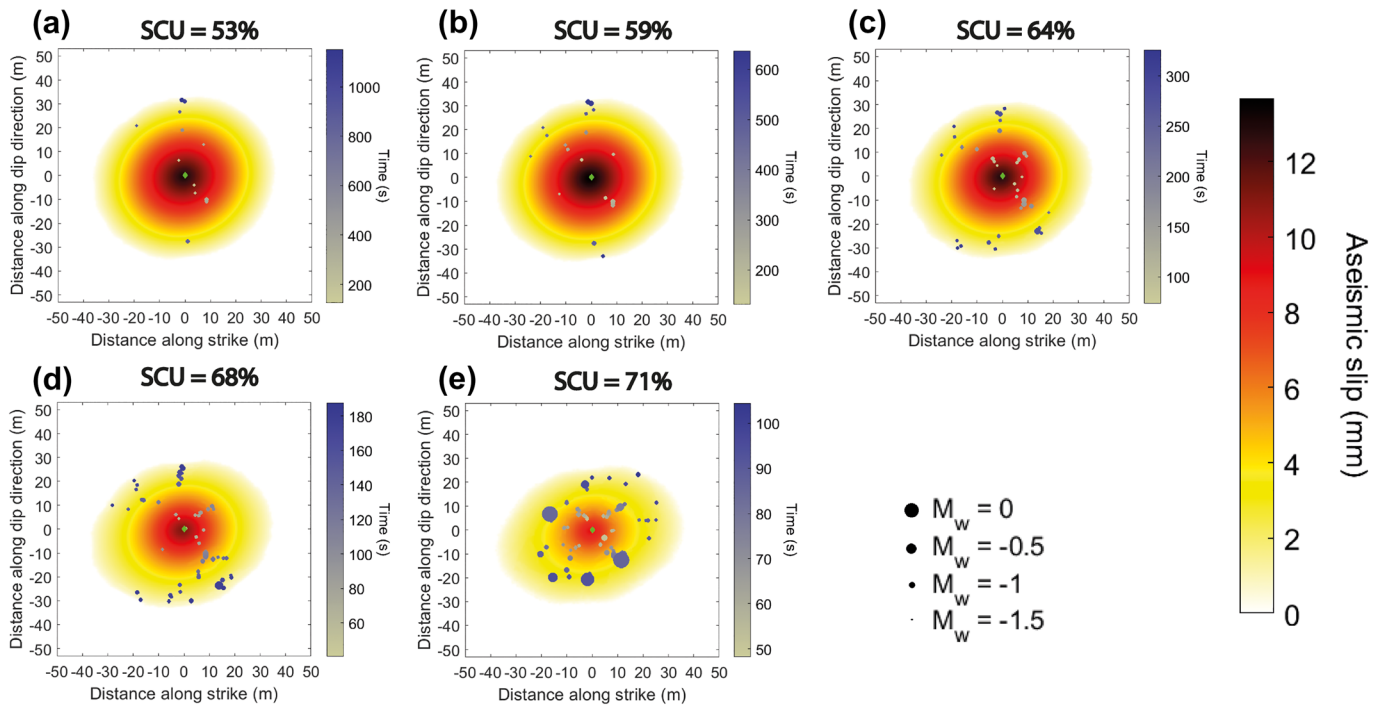


**Figure 7.** (a–e) Aseismic slip across the fault for different initial fault criticality defined with SCU equals to (a) 53%, (b) 59%, (c) 64%, (d) 68%, and (e) 71%, respectively. The location and moment magnitude of each event are represented with a colored circle. The size of circles represents the event magnitude.

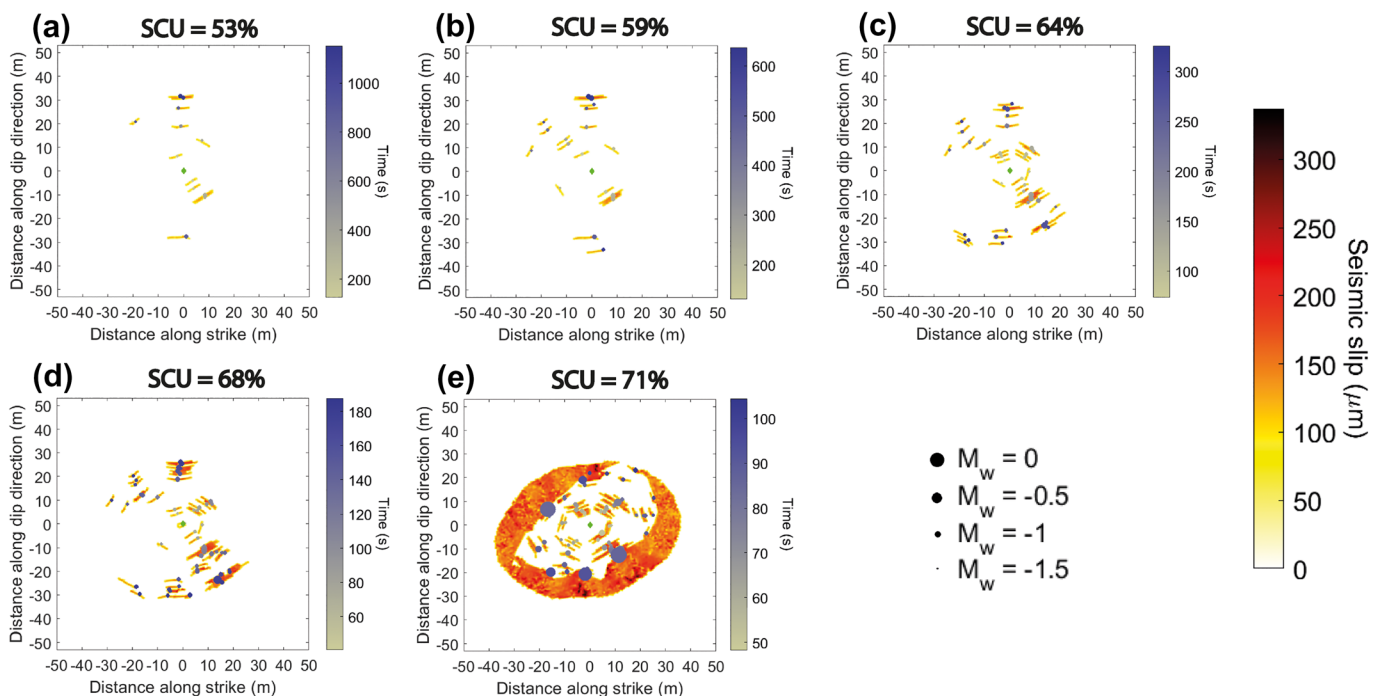


**Figure 8.** (a–d) Seismic slip across the fault for different initial fault criticality defined with SCU equals to (a) 53%, (b) 59%, (c) 64%, (d) 68%, and (e) 71%, respectively. The location and moment magnitude of each event are represented with a colored circle. The size of circles represents the event magnitude.

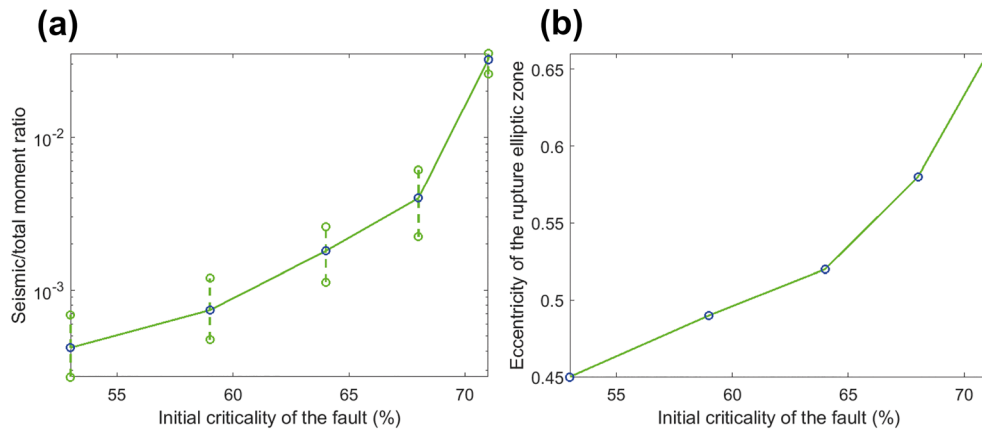


**Figure 9.** Sensitivity of (a) the ratio of the seismic to total moment, and (b) the shape of the ruptured area expressed by the eccentricity of the elliptical rupture to the initial fault criticality defined with SCU equal to 53%, 59%, 64%, 68%, and 71%, respectively. The dashed lines at constant criticality represents the range of values of seismic-to-total moment ratio adopted by a variation of 10% of the slip velocity threshold.

direction of  $\vec{\tau}$ . To quantify the shape of the final rupture, we approximate it as an ellipse and compute the eccentricity ( $e$ ) using the large semiaxis ( $a$ ) and the small semiaxis ( $b$ ):

$$e = \sqrt{1 - \left(\frac{b}{a}\right)^2} \quad (17)$$

This parameter is 0 for a circle and approaches 1 for a very thin ellipse. Figure 9b indicates that the eccentricity of the final slip increases with closeness to failure, from 0.46 for SCU of 53% to 0.64 for SCU of 73%.

These simulations were performed without shear-induced dilation. However, taking account dilation has only a minor effect on the seismicity and rupture fronts, especially at high SCU (see supporting information, Figure S1). We also test the influence of the coupling between permeability changes and fluid pressure on aseismic slip and seismicity distribution on the fault (Figures S3 and S4). If not considered, the number of earthquakes increases between 2% and 50%, as well as the cumulative seismic moment. The seismicity migration velocity is also amplified by up to 25%. The pressure front is not modified by the presence or absence of coupling between permeability variations and pressure.

#### 4. Discussion

This study presents numerical simulations of the coupled seismo-hydro-mechanical response of a permeable, slip-weakening fault in which fluid is injected, to investigate the relationship between fluid injection and characteristics of the resulting seismicity sequences. While the simple single fault geometry may not be a complete representation of a natural system, the simulated seismic catalogs exhibit a number of features that are observed in real sequences of induced seismicity. Based on simulations spanning a range of initial closeness to failure, we identified the following main results:

1. The deformation is dominantly aseismic. The seismic-to-aseismic ratio increases with distance to the injection point. The largest seismic events occurred far from the injection point.
2. The rupture and the seismicity may outpace the pressurized zone. This behavior is more favored in faults that are initially closer to failure.
3. The rupture extent and shape, the amplitude of aseismic slip, and the number and magnitude of seismic events are strongly influenced by the initial prestress condition.
4. The seismicity front follows the shear stress front, and not the fluid pressure front.
5. The seismicity migration velocity accelerates when the shear stress front outpaces the fluid pressure front.

These results are broadly in agreement with observations in the laboratory (Goodfellow et al., 2015) and in situ experiments (De Barros et al., 2016; Duboeuf et al., 2017; Guglielmi et al., 2015), in reservoir stimulation

(Eyre et al., 2019; Wei et al., 2015), and theoretical studies (Bhattacharya & Viesca, 2019; Cappa et al., 2019). Understanding the conditions for seismic and aseismic fault slip is important to study the magnitude and distribution of seismicity that can occur during fluid injection. In the following, we discuss the implications of our results for induced seismicity in the light of observations of real data and previous modeling.

#### 4.1. Rupture Is Mainly Aseismic During Injection

Our numerical simulation results show that the fault rupture is dominantly aseismic during the injection. This behavior is mainly controlled by the prestress conditions, and the initial high-permeability of the fault which favors the fluid pressure to diffuse across the fault. We observed that lower prestress and shear-induced dilation favor aseismic slip. The seismic-to-aseismic ratio varied between 0.05% and 4% with increasing closeness to failure. Such values are consistent with field measurements acquired in decametric scale experiments (De Barros et al., 2019), in the laboratory (Goodfellow et al., 2015) and during reservoir stimulations (e.g., Calò et al., 2011; Schmittbuhl et al., 2014).

The results of our simulations also show that the slipping area around the injection point is nearly devoid of seismic events. This is consistent with seismological observations in in situ injection experiments (De Barros et al., 2016; Duboeuf et al., 2017). In our models, even though all grid points reach seismic slip velocities inside the ruptured patch, they lead to very small, separated seismic events near the injection. These events have a slipping patch less than 1.5 m<sup>2</sup> and thus are discarded from our analysis, as mentioned in section 3.1. Indeed, such small events do not rupture a minimum surface area over a same time window, preventing the nucleation of large seismic rupture near the injection point. Furthermore, models indicate that the magnitude, the number of seismic events and the seismic-to-aseismic ratio increase with the distance to the injection point, consistently with observations of induced earthquake sequences (Eyre et al., 2019; Hopp et al., 2019).

Since the seismic part of the rupture is small in our models, the stress perturbation due to aseismic slip is important and the transition from aseismic to seismic slip is mainly controlled by local stressing rate and friction weakening over short distances. Stress transfer due to the expansion of the aseismic slip zone plays a key role, whereas fluid pressure increase is not necessary to trigger rupture outside the stimulation zone. Therefore, although a large increase in fluid pressure occurs near the injection, the shear stress increase and the friction weakening are responsible for the change in fault strength and stability conditions. Thus, the perturbation of the shear stress due to aseismic fault slip is crucial in injection-induced seismicity. Due to the stress redistribution, aseismic slip on an individual patch may cause shear stress increase on neighboring patches, thus potentially triggering individual or cascading seismic ruptures.

#### 4.2. Rupture Outpaces the Fluid Pressure Front

Our modeling results show that the shear stress front, and thus the rupture front, eventually outpaces the fluid pressure front on faults that are initially close to failure. The expansion of the aseismic slip region allows the development of pronounced shear stress that propagates outward from the main stimulation zone. This propagating stress increase can cause the nucleation of seismic events at the edge of the aseismic slipping zone. This process of an aseismic slip outpacing the pressure front has been previously proposed in experiments (Cappa et al., 2019; De Barros et al., 2016, 2018; Guglielmi et al., 2015) and models (Bhattacharya & Viesca, 2019; Cappa et al., 2018, 2019; Eyre et al., 2019; Garagash & Germanovich, 2012; Gischig, 2015). Bhattacharya and Viesca (2019) have recently showed in a model used to fit the data of Guglielmi et al. (2015) that the rupture front can outpace the fluid pressure front when the fault is nearly critically stressed and large overpressure is sustained over the duration of injection. Their model shows a behavior of the rupture front different from a fluid-driven diffusion. Our model results provide similar conclusions, with the aseismic rupture front diffusing either behind or beyond the pressure front depending on the fault closeness to failure. In addition, we also observed in our models that the shear stress front strongly accelerates when it outpaces the fluid pressure front for large fault criticalities. This acceleration leads to two phases of seismic migration. Therefore, the combination of permeability increase and friction weakening behind the rupture front in our model enables a stress drop to occur outside the pressurized zone, providing the necessary energy to drive and accelerate the rupture beyond the pressure front.

If the fault is initially far from failure, once the slip is initiated, the shear stress front is arrested behind or near the limit of the pressurized front. Thus, the SCU of the fault influences the position of the shear

stress front relative to the fluid pressure front. The overpressure and its diffusion across the fault seem to play a secondary role in the rupture evolution, especially at a distance to the injection point where the energy due to fluid overpressure decays. This result is in agreement with previous modeling studies, both for a pressurized fault with slip-weakening friction (Galis et al., 2017) and rate-and-state friction (Gischig, 2015).

### 4.3. Seismicity Migration

In numerous studies, the seismicity front is thought to be directly linked to the fluid pressure diffusion (e.g., Shapiro et al., 1997, 2002), but other studies show that the pure diffusion model does not fully capture the effect of the stress interaction (Cornet, 2000; Duboeuf et al., 2017). Here, we observed that the seismicity front follows the shear stress front, and thus the rupture front, whatever the initial closeness to failure. On faults far from failure, or at the beginning of injection on faults closer to failure, the seismicity front lags behind the pressure front. On faults close to failure, seismicity occurs outside the pressurized area due to the aseismic rupture front outpacing the fluid pressure front. Thus, seismic events are mainly triggered by the shear stress increase associated with the expansion of the aseismic slip rather than by the direct weakening effect of the fluid pressure. As the seismicity front may be far beyond the pressure front, analytical solutions using a constant hydraulic diffusivity in a homogeneous, isotropic, porous medium (e.g., Shapiro et al., 1997, 2002) cannot be applied, because they ignore the significant impact of the shear stress increases due to the approach of the aseismic slip front, followed by a shear stress drop related to friction weakening.

Additionally, our models showed that in a critically stressed fault, seismicity migration at large time and distance to the injection point showed an acceleration due to aseismic slip acceleration. Such acceleration phases have been observed in a few reservoir injection sites, like in Basel (Goertz-Allmann et al., 2011) or in the area of Jones, in Oklahoma (Keranen et al., 2014). For instance, Goertz-Allmann et al. (2011) showed that for the Basel geothermal site, the theoretical pore pressure expected for the far events is very small, less than 1 MPa. Later, Catalli et al. (2016) demonstrated that most seismic events during the Basel stimulation were triggered by stress transfer due to earthquake interactions. Such migration of an expanding aseismic region may be also interpreted as quasi-linear seismicity patterns (almost constant migration speed), that have been previously observed at the Rittershoffen geothermal site in France (Lengliné et al., 2017) and during the 2003–2004 Corinth Gulf swarm in Greece (Duverger et al., 2015). As observed in Figure 6, the transition from a quasi-linear to an accelerating migration velocity depends on the difference between the initial stress state and the residual shear stress  $\mu_d \sigma_n$  (e.g., Galis et al., 2017). If the difference, called background stress drop, is negative, the rupture will be stabilized and thus cannot accelerate, as observed in simulations with SCU less or equal to 64%. This is also observed in velocity-strengthening rate-and-state models (Dublanche, 2019b). Furthermore, our models indicated that the migration velocity of the seismicity changes with the fault closeness to failure.

Therefore, pressure-only models are insufficient to evaluate the spatiotemporal evolution of induced earthquakes because other physical processes (e.g., aseismic slip and static stress transfer) in addition to fluid pressure diffusion contribute to the evolution of seismicity. In turn, our results suggest that observed migration patterns of induced seismicity cannot be used directly to infer fluid diffusivity. This highlights the importance of accounting for the interactions between the different physical processes because, although referred to as induced seismicity, our models indicate that seismic events are mainly triggered by shear stress increase as opposed to induced by fluid pressure.

### 4.4. Modeling Limitations

Our modeling accounts for important processes involved during fluid-induced seismicity, including fluid flow, hydromechanical coupling, aseismic slip and seismic rupture. The mutual interactions between these processes increase the understanding of the physics and the behavior of induced seismicity. However, in our modeling approach some simplifications have been made.

We considered a simplified model geometry with a single fault. This class of models is useful to explore coupled processes. However, natural systems are often composed of a network of faults and interconnected fractures. Considering multiple faults with different orientations would help to represent a variety of slip behaviors. This may be particularly important in evaluations of the spatiotemporal evolution of induced sequences containing characteristics which arise due to fault interaction and off-fault seismicity. Despite the single-fault assumption, our model is inherently discrete and thus represents a collection of

interacting fault patches that can fail independently. Comparing this class of models to continuum models involving fracture mechanics theory (Galís et al., 2017) or simulations with explicit heterogeneities or secondary faults (e.g., Luo & Ampuero, 2017) are important tasks for further research.

The imposed uniform distribution of hydromechanical and frictional properties across the fault is also a simplification. In natural settings, these fault properties are heterogeneously distributed and the rock properties surrounding the fault can be dissimilar. This results in a more variable fluid pressure and stress distribution. Fluid pressure can diffuse in the fault along channels separated by rock bridges that can transmit local shear stress which may potentially generate seismic ruptures. For instance, previous studies have shown that changes and spatial variations in fault permeability can influence the timing and location of induced seismicity (Chang & Segall, 2016; McNamara et al., 2015; Norbeck & Horne, 2016; Yeck et al., 2016; Zhang et al., 2013). The evolution and spatial distribution of frictional parameters are also known to affect the slip mode (aseismic versus seismic) of the fault and the earthquake source characteristics. To model friction, here we have used a linear slip-weakening friction law, which is a simplified model for the simulation of fault slip and earthquake rupture. Laboratory experiments (e.g., Marone, 1998) and theoretical studies (e.g., Ampuero & Rubin, 2008) have shown that friction evolution, especially at low slip rates relevant for aseismic deformation, can be described by the rate-and-state friction law, which can reproduce a large spectrum of fault slip behaviors over a range of slip velocity and time not captured with a slip-weakening friction. Further research on the influence of fault frictional and hydromechanical properties and behaviors is necessary to estimate their impact on the rupture modes and the spatiotemporal evolution of sequences of induced earthquakes, especially irregular sequences of events with different magnitudes (Almakari et al., 2019).

Moreover, the migration velocities observed in our simulations are far larger than those observed on the field. Indeed, the velocities we observe for stress-driven seismicity are between 360 m/hr and 1.5 km/hr, while the migration speed is of 15 m/hr at Rittershoffen (Lengliné et al., 2017) and between 3 and 10 m/hr in Basel and in the area of Jones, Oklahoma (Goertz-Allmann et al., 2011; Keranen et al., 2014). This scale difference in migration velocity may be due to the difference of a few orders of magnitude in permeability between our simulations and in situ observations. The high level of pressure may also play a role in such high seismic migration velocities, as well as the simplified geometry considered in our model.

Finally, we have tested only one injection protocol in this study. Nonetheless, previous studies have demonstrated that the rate and magnitude of injection-induced seismicity depends on the chosen injection scenario (Almakari et al., 2019; Aochi et al., 2014; Passelègue et al., 2018). Further understanding of the effect of injection characteristics (rate, magnitude, shape, and duration) on the resulting seismicity and aseismic fault slip is crucial.

## 5. Conclusion

The main objective of this study is to examine the effects of a fluid injection in a permeable fault, located at the typical depth of subsurface reservoirs, on the spatiotemporal evolution of induced seismicity and aseismic slip, and their mutual interactions. We address this question numerically with three-dimensional two-way coupled hydromechanical simulations of an inherently discrete earthquake fault model governed by a slip-weakening friction law. Simulations spanning a range of prestress conditions produce synthetic seismicity catalogs. The simulations of a generic case show how the combined effect of fluid pressure and shear stress change can generate and propagate aseismic slip and seismic events across a fault, consistently with observations of induced seismicity sequences in field experiments and in natural systems.

Through our investigations, we show that the location of seismic events is not limited to the pressurized region and that the earthquakes are triggered beyond the pressure front by the shear stress increase at the edge of the propagating aseismic slip zone. This behavior is consistent with previous field observations (De Barros et al., 2018; Eyre et al., 2019; Guglielmi et al., 2015; Wei et al., 2015) and theoretical studies (Bhattacharya & Viesca, 2019; Cappa et al., 2019). Moreover, our results indicate that the seismicity migration follows the evolution of the shear stress front rather than the fluid pressure diffusion front, whatever the initial closeness to failure of the fault. In faults initially far from failure, the seismicity and the shear stress front develop behind the pressure front, and the migration of seismicity has a mean velocity that increases with increasing prestress. In faults close to failure, once the shear stress front outpaces the fluid pressure front, the seismicity migration accelerates. This acceleration is associated with the acceleration of the

aseismic rupture front. Thus, the initial closeness to failure, fault frictional properties, and the shear stress increase accompanying the expansion of the aseismic slip area are more significant than the direct effects of the fluid pressure diffusion in controlling the triggering and growth of seismicity during fluid injection.

Given its practical implications, the spatiotemporal evolution of the seismicity front is a good probe for the shear stress perturbation accompanying the expansion of aseismic slip, behind and beyond the pressurized zone. Therefore, the monitoring of aseismic slip during fluid injection, using techniques based on geodesy or seismic velocity changes (Rivet et al., 2016; Shirzaei et al., 2016; Wei et al., 2015), could be useful to anticipate the evolution of potentially seismic areas in and outside the stimulation zone.

### Acknowledgments

This work has been supported by the French government, through the HYDROSEIS project under Contract ANR-13-JS06-0004-01 (F. Cappa) and through the UCAJEDI Investments in the Future project managed by the National Research Agency (ANR) with the reference number ANR-15-IDEX-01. We also thank the Observatoire de la Côte d'Azur for supporting this research through BQR OCA. F. Cappa acknowledges support from the Institut Universitaire de France. N. Wynants-Morel benefits from a financial support of the Université Côte d'Azur (UCA). We thank Martijn van den Ende, Jim Hazzard, and Robert Viesca for fruitful discussions. We also thank the Editor, Yehuda Ben-Zion, Pierre Dublanche, and Pathikrit Bhattacharya for constructive comments during the review process. No data was used in this study.

### References

- Almakari, M., Dublanche, P., Chauris, H., & Pellet, F. (2019). Effect of the injection scenario on the rate and magnitude content of injection-induced seismicity: Case of a heterogeneous fault. *Journal of Geophysical Research: Solid Earth*, *124*, 8426–8448. <https://doi.org/10.1029/2019JB017898>
- Ampuero, J.-P., & Rubin, A. M. (2008). Earthquake nucleation on rate and state faults—Aging and slip laws. *Journal of Geophysical Research*, *113*, B01302. <https://doi.org/10.1029/2007JB005082>
- Ampuero, J.-P., Vilotte, J.-P., & Sánchez-Sesma, F. J. (2002). Nucleation of rupture under slip dependent friction law: Simple models of fault zone. *Journal of Geophysical Research*, *107*(B12), 2324. <https://doi.org/10.1029/2001JB000452>
- Aochi, H., Poisson, B., Toussaint, R., Rachez, X., & Schmittbuhl, J. (2014). Self-induced seismicity due to fluid circulation along faults. *Geophysical Journal International*, *196*(3), 1544–1563. <https://doi.org/10.1093/gji/ggt356>
- Baisch, S., Vörös, R., Rother, E., Stang, H., Jung, R., & Schellschmidt, R. (2010). A numerical model for fluid injection induced seismicity at Soultz-sous-Forêts. *International Journal of Rock Mechanics and Mining Sciences*, *47*(3), 405–413. <https://doi.org/10.1016/j.ijrmms.2009.10.001>
- Bao, X., & Eaton, D. W. (2016). Fault activation by hydraulic fracturing in western Canada. *Science*, *354*(6318), 1406–1409. <https://doi.org/10.1126/science.aag2583>
- Barbour, A. J., Norbeck, J. H., & Rubinstein, J. L. (2017). The effects of varying injection rates in Osage County, Oklahoma, on the 2016  $M_w$  5.8 Pawnee earthquake. *Seismological Research Letters*, *88*(4), 1040–1053. <https://doi.org/10.1785/0220170003>
- Ben-Zion, Y. (2008). Collective behavior of earthquakes and faults: Continuum-discrete transitions, progressive evolutionary changes, and different dynamic regimes. *Reviews of Geophysics*, *46*, RG4006. <https://doi.org/10.1029/2008RG000260>
- Ben-Zion, Y. (2012). Episodic tremor and slip on a frictional interface with critical zero weakening in elastic solid. *Geophysical Journal International*, *189*(2), 1159–1168. <https://doi.org/10.1111/j.1365-246X.2012.05422.x>
- Ben-Zion, Y., & Rice, J. R. (1993). Earthquake failure sequences along a cellular fault zone in a three-dimensional elastic solid containing aseismic and nonasperity regions. *Journal of Geophysical Research*, *98*(B8), 14,109–14,131. <https://doi.org/10.1029/93JB01096>
- Ben-Zion, Y., & Rice, J. R. (1995). Slip patterns and earthquake populations along different classes of faults in elastic solids. *Journal of Geophysical Research*, *100*(B7), 12,959–12,983. <https://doi.org/10.1029/94JB03037>
- Bhattacharya, P., & Viesca, R. C. (2019). Fluid-induced aseismic fault slip outpaces pore-fluid migration. *Science*, *364*(6439), 464–468. <https://doi.org/10.1126/science.aaw7354>
- Brown, D. (1989). The flow of water and displacement of hydrocarbons in fractured chalk reservoirs. In J. C. Goff, & B. P. Williams (Eds.), *FluidFlow in sedimentary basins and aquifers*, (pp. 201–218). London: Geological Society.
- Buijze, L., van den Bogert, P., Wassing, B. B. T., & Orlic, B. (2019). Nucleation and arrest of dynamic rupture induced by reservoir depletion. *Journal of Geophysical Research: Solid Earth*, *124*, 3620–3645. <https://doi.org/10.1029/2018JB016941>
- Buijze, L., van den Bogert, P. A. J., Wassing, B. B. T., Orlic, B., & ten Veen, J. (2017). Fault reactivation mechanisms and dynamic rupture modelling of depletion-induced seismic events in a Rotliegendes gas reservoir. *Netherlands Journal of Geosciences*, *96*(5), s131–s148. <https://doi.org/10.1017/njg.2017.27>
- Byerlee, J. (1978). Friction of rocks. *Pure and Applied Geophysics PAGEOPH*, *116*(4-5), 615–626. <https://doi.org/10.1007/BF00876528>
- Calò, M., Dorbath, C., Cornet, F. H., & Cuenot, N. (2011). Large-scale aseismic motion identified through 4-D P-wave tomography. *Geophysical Journal International*, *186*(3), 1295–1314. <https://doi.org/10.1111/j.1365-246X.2011.05108.x>
- Candela, T., Osinga, S., Ampuero, J., Wassing, B., Pluymaekers, M., Fokker, P. A., et al. (2019). Depletion-induced seismicity at the Groningen gas field: Coulomb rate-and-state models including differential compaction effect. *Journal of Geophysical Research: Solid Earth*, *124*, 7081–7104. <https://doi.org/10.1029/2018JB016670>
- Cappa, F., Guglielmi, Y., Nussbaum, C., & Birkholzer, J. (2018). On the relationship between fault permeability increases, induced stress perturbation, and the growth of aseismic slip during fluid injection. *Geophysical Research Letters*, *45*. <https://doi.org/10.1029/2018GL080233>
- Cappa, F., & Rutqvist, J. (2011). Impact of CO<sub>2</sub> geological sequestration on the nucleation of earthquakes. *Geophysical Research Letters*, *38*, L17313. <https://doi.org/10.1029/2011GL048487>
- Cappa, F., & Rutqvist, J. (2012). Seismic rupture and ground accelerations induced by CO<sub>2</sub> injection in the shallow crust. *Geophysical Journal International*, *190*, 1784–1789. <https://doi.org/10.1111/j.1365-246X.2012.05606.x>
- Cappa, F., Scuderi, M. M., Collettini, C., Guglielmi, Y., & Avouac, J.-P. (2019). Stabilization of fault slip by fluid injection in the laboratory and in situ. *Science Advances*, *5*, eaau4065. <https://doi.org/10.1126/sciadv.aau4065>
- Carlson, J. M., & Langer, J. S. (1989a). Mechanical model of an earthquake fault. *Physical Review A*, *40*(11), 6470–6484. <https://doi.org/10.1103/PhysRevA.40.6470>
- Carlson, J. M., & Langer, J. S. (1989b). Properties of earthquakes generated by fault dynamics. *Physical Review Letters*, *62*(22), 2632–2635. <https://doi.org/10.1103/PhysRevLett.62.2632>
- Catalli, F., Rinaldi, A. P., Gischig, V., Nespoli, M., & Wiemer, S. (2016). The importance of earthquake interactions for injection-induced seismicity: Retrospective modeling of the Basel enhanced geothermal system. *Geophysical Research Letters*, *43*, 4992–4999. <https://doi.org/10.1002/2016GL068932>
- Chang, K. W., & Segall, P. (2016). Injection-induced seismicity on basement faults including poroelastic stressing. *Journal of Geophysical Research: Solid Earth*, *121*, 2708–2726. <https://doi.org/10.1002/2015JB012561>

- Ciarro, F., & Lecampion, B. (2019). Effect of Dilatancy on the transition from aseismic to seismic slip due to fluid injection in a fault. *Journal of Geophysical Research: Solid Earth*, *124*, 3724–3743. <https://doi.org/10.1029/2018JB016636>
- Clarke, H., Eisner, L., Styles, P., & Turner, P. (2014). Felt seismicity associated with shale gas hydraulic fracturing: The first documented example in Europe. *Geophysical Research Letters*, *41*, 8308–8314. <https://doi.org/10.1002/2014GL062047>
- Cochard, A., & Madariaga, R. (1994). Dynamic faulting under rate-dependent friction. *Pure and Applied Geophysics Pageoph*, *142*(3-4), 419–445. <https://doi.org/10.1007/BF00876049>
- Cornet, F. H. (2000). Comment on 'Large-scale in situ permeability tensor of rocks from induced microseismicity' by S. A. Shapiro, P. Audigane, and J.-J. Royer. *Geophysical Journal International*, *140*, 465–469
- Cornet, F. H. (2012). The relationship between seismic and aseismic motions induced by forced fluid injections. *Hydrogeology Journal*, *20*(8), 1463–1466. <https://doi.org/10.1007/s10040-012-0901-z>
- Cornet, F. H. (2016). Seismic and aseismic motions generated by fluid injections. *Geomechanics for Energy and the Environment*, *5*, 42–54. <https://doi.org/10.1016/j.gete.2015.12.003>
- Cornet, F. H., Helm, J., Poitrenaud, H., & Etchecopar, A. (1997). Seismic and aseismic slips induced by large-scale fluid injections. *Pure and Applied Geophysics*, *150*(3-4), 563–583. <https://doi.org/10.1007/s000240050093>
- Cundall, P. A. (1988). Formulation of a three-dimensional distinct element model—Part I. A scheme to detect and represent contacts in a system composed of many polyhedral blocks. *International Journal of Rock Mechanics and Mining Science and Geomechanics Abstracts*, *25*(3), 107–116. [https://doi.org/10.1016/0148-9062\(88\)92293-0](https://doi.org/10.1016/0148-9062(88)92293-0)
- De Barros, L., Cappa, F., Guglielmi, Y., Duboeuf, L., & Grasso, J.-R. (2019). Energy of injection-induced seismicity predicted from in-situ experiments. *Scientific Reports*, *9*(1), 4999. <https://doi.org/10.1038/s41598-019-41306-x>
- De Barros, L., Daniel, G., Guglielmi, Y., Rivet, D., Caron, H., Payre, X., et al. (2016). Fault structure, stress, or pressure control of the seismicity in shale? Insights from a controlled experiment of fluid-induced fault reactivation. *Journal of Geophysical Research: Solid Earth*, *121*, 4506–4522. <https://doi.org/10.1002/2015JB012633>
- De Barros, L., Guglielmi, Y., Rivet, D., Cappa, F., & Duboeuf, L. (2018). Seismicity and fault aseismic deformation caused by fluid injection in decametric in-situ experiments. *Comptes Rendus Geoscience*, *350*(8), 464–475. <https://doi.org/10.1016/j.crte.2018.08.002>
- Dublanchet, P. (2019a). Scaling and variability of interacting repeating earthquake sequences controlled by asperity density. *Geophysical Research Letters*, *46*, 11,950–11,958. <https://doi.org/10.1029/2019GL084614>
- Dublanchet, P. (2019b). Fluid driven shear cracks on a strengthening rate-and-state frictional fault. *Journal of the Mechanics and Physics of Solids*, *132*, 103,672.
- Duboeuf, L., De Barros, L., Cappa, F., Guglielmi, Y., Deschamps, A., & Seguy, S. (2017). Aseismic motions drive a sparse seismicity during fluid injections into a fractured zone in a carbonate reservoir. *Journal of Geophysical Research: Solid Earth*, *122*, 8285–8304. <https://doi.org/10.1002/2017JB014535>
- Duverger, C., Godano, M., Bernard, P., Lyon-Caen, H., & Lambotte, S. (2015). The 2003–2004 seismic swarm in the western Corinth rift: Evidence for a multiscale pore pressure diffusion process along a permeable fault system. *Geophysical Research Letters*, *42*, 7374–7382. <https://doi.org/10.1002/2015GL065298>
- Ellsworth, W. L. (2013). Injection-induced earthquakes. *Science*, *341*(6142), 1225942. <https://doi.org/10.1126/science.1225942>
- Eyre, T. S., Eaton, D. W., Garagash, D. I., Zecevic, M., Venieri, M., Weir, R., & Lawton, D. C. (2019). The role of aseismic-slip in hydraulic fracturing-induced seismicity. *Science Advances*, *5*(8), eaav7172. <https://doi.org/10.1126/sciadv.aav7172>
- Galis, M., Ampuero, J. P., Mai, P. M., & Cappa, F. (2017). Induced seismicity provides insight into why earthquake ruptures stop. *Science Advances*, *3*, eaap7528. <https://doi.org/10.1126/sciadv.aap7528>
- Galis, M., Ampuero, J.-P., Mai, P. M., & Kristek, J. (2019). Initiation and arrest of earthquake ruptures due to elongated overstressed regions. *Geophysical Journal International*, *217*(3), 1783–1797. <https://doi.org/10.1093/gji/ggz086>
- Garagash, D. I., & Germanovich, L. N. (2012). Nucleation and arrest of dynamic slip on a pressurized fault. *Journal of Geophysical Research*, *117*, B10310. <https://doi.org/10.1029/2012JB009209>
- Gischig, V. S. (2015). Rupture propagation behavior and the largest possible earthquake induced by fluid injection into deep reservoirs. *Geophysical Research Letters*, *42*, 7420–7428. <https://doi.org/10.1002/2015GL065072>
- Goebel, T. H. W., Hosseini, S. M., Cappa, F., Hauksson, E., Ampuero, J. P., Aminzadeh, F., & Saleeby, J. B. (2016). Wastewater disposal and earthquake swarm activity at the southern end of the Central Valley, California. *Geophysical Research Letters*, *43*, 1092–1099. <https://doi.org/10.1002/2015GL066948>
- Goebel, T. H. W., Weingarten, M., Chen, X., Haffener, J., & Brodsky, E. E. (2017). The 2016 Mw 5.1 Fairview, Oklahoma earthquakes: Evidence for long-range poroelastic triggering at >40 km from fluid disposal wells. *Earth planet. Science Letters*, *472*, 50–61. <https://doi.org/10.1016/j.epsl.2017.05.011>
- Goertz-Allmann, B. P., Goertz, A., & Wiemer, S. (2011). Stress drop variations of induced earthquakes at the Basel geothermal site. *Geophysical Research Letters*, *38*, L09308. <https://doi.org/10.1029/2011GL047498>
- Goodfellow, S. D., Nasser, M. H. B., Maxwell, S. C., & Young, R. P. (2015). Hydraulic fracture energy budget: Insights from the laboratory. *Geophysical Research Letters*, *42*, 3179–3187. <https://doi.org/10.1002/2015GL063093>
- Grigoli, F., Cesca, S., Rinaldi, A. P., Manconi, A., López-Comino, J. A., Clinton, J. F., et al. (2018). The November 2017 Mw 5.5 Pohang earthquake: A possible case of induced seismicity in South Korea. *Science*, *360*(6392), 1003–1006. <https://doi.org/10.1126/science.aat2010>
- Guglielmi, Y., Cappa, F., & Amitrano, D. (2008). High-definition analysis of fluid-induced seismicity related to the mesoscale hydromechanical properties of a fault zone. *Geophysical Research Letters*, *35*, L06306. <https://doi.org/10.1029/2007GL033087>
- Guglielmi, Y., Cappa, F., Avouac, J.-P., Henry, P., & Elsworth, D. (2015). Seismicity triggered by fluid injection-induced aseismic slip. *Science*, *348*(6240), 1224–1226. <https://doi.org/10.1126/science.aab0476>
- Holland, A. A. (2013). Earthquakes triggered by hydraulic fracturing in south-Central Oklahoma. *Bulletin of the Seismological Society of America*, *103*(3), 1784–1792. <https://doi.org/10.1785/0120120109>
- Hopp, C., Sewell, S., Mroczek, S., Savage, M., & Townend, J. (2019). Seismic response to injection well stimulation in a high-temperature, high-permeability reservoir. *Geochemistry, Geophysics, Geosystems*, *20*, 2848–2871. <https://doi.org/10.1029/2019GC008243>
- Huang, Y., De Barros, L., & Cappa, F. (2019). Illuminating the rupturing of microseismic sources in an injection-induced earthquake experiment. *Geophysical Research Letters*, *46*, 9563–9572. <https://doi.org/10.1029/2019GL083856>
- Hubbert, M., & Rubey, W. W. (1959). Role of fluid pressure in mechanics of overthrust faulting. *Geological Society of America Bulletin*, *70*(2), 115. [https://doi.org/10.1130/0016-7606\(1959\)70\[115:ROFPIM\]2.0.CO;2](https://doi.org/10.1130/0016-7606(1959)70[115:ROFPIM]2.0.CO;2)
- Ida, Y. (1972). Cohesive force across the tip of a longitudinal-shear crack and Griffith's specific surface energy. *Journal of Geophysical Research*, *77*(20), 3796–3805. <https://doi.org/10.1029/JB077i020p03796>

- Itasca Consulting Group, Inc., (2016). 3DEC—Three-dimensional distinct element code. Minneapolis: Itasca.
- Izadi, G., & Elsworth, D. (2015). The influence of thermal-hydraulic-mechanical- and chemical effects on the evolution of permeability, seismicity and heat production in geothermal reservoirs. *Geothermics*, 53, 385–395. <https://doi.org/10.1016/j.geothermics.2014.08.005>
- Jaeger, J. C., & Cook, N. G. (1984). *Fundamentals of rock mechanics* (3rd ed., repr. ed, Science paperbacks). London, UK: Chapman and Hall.
- Jeanne, P., Guglielmi, Y., Lamarche, J., Cappa, F., & Marié, L. (2012). Architectural characteristics and petrophysical properties evolution of a strike-slip fault zone in a fractured porous carbonate reservoir. *Journal of Structural Geology*, 44, 93–109. <https://doi.org/10.1016/j.jsg.2012.08.016>
- Jin, L., & Zoback, M. D. (2018a). *Modeling induced seismicity: Co-seismic fully dynamic spontaneous rupture considering fault Poroelastic stress*. Paper presented at the 52th US Rock Mechanics/Geomechanics Symposium, American Rock Mechanics Association (ARMA), Seattle, WA.
- Jin, L., & Zoback, M. D. (2018b). *Hydromechanical–stochastic modeling of fluid-induced seismicity in fractured poroelastic media*. <https://doi.org/10.31223/osf.io/8ynm7>
- Keranen, K. M., Savage, H. M., Abers, G. A., & Cochran, E. S. (2013). Potentially induced earthquakes in Oklahoma, USA: Links between wastewater injection and the 2011 Mw 5.7 earthquake sequence. *Geology*, 41(6), 699–702. <https://doi.org/10.1130/G34045.1>
- Keranen, K. M., & Weingarten, M. (2018). Induced seismicity. *Annual Review of Earth and Planetary Sciences*, 46(1), 149–174. <https://doi.org/10.1146/annurev-earth-082517-010054>
- Keranen, K. M., Weingarten, M., Abers, G. A., Bekins, B. A., & Ge, S. (2014). Sharp increase in Central Oklahoma seismicity since 2008 induced by massive wastewater injection. *Science*, 345(6195), 448–451. <https://doi.org/10.1126/science.1255802>
- Kim, K.-H., Ree, J.-H., Kim, Y., Kim, S., Kang, S. Y., & Seo, W. (2018). Assessing whether the 2017  $M_w$  5.4 Pohang earthquake in South Korea was an induced event. *Science*, 360(6392), 1007–1009. <https://doi.org/10.1126/science.aat6081>
- Kwiatk, G., Saarno, T., Ader, T., Bluemle, F., Bohnhoff, M., Chendorain, M., et al. (2019). Controlling fluid-induced seismicity during a 6.1-km-deep geothermal stimulation in Finland. *Science Advances*, 5, eaav7224. <https://doi.org/10.1126/sciadv.aav7224>
- Lee, K.-K., Ellsworth, W. L., Giardini, D., Townend, J., Ge, S., Shimamoto, T., et al. (2019). Managing injection-induced seismic risks. *Science*, 364(6442), 730–732. <https://doi.org/10.1126/science.aax1878>
- Lengliné, O., Boubacar, M., & Schmittbuhl, J. (2017). Seismicity related to the hydraulic stimulation of GRT1, Rittershoffen, France. *Geophysical Journal International*, ggw490. <https://doi.org/10.1093/gji/ggw490>
- Lui, S. K. Y., & Lapusta, N. (2016). Repeating microearthquake sequences interact predominantly through postseismic slip. *Nature Communications*, 7(1), 13020. <https://doi.org/10.1038/ncomms13020>
- Luo, Y., & Ampuero, J.-P. (2017). *Preprint: Tremor migration patterns and the collective behavior of deep asperities mediated by creep*. <https://doi.org/10.31223/osf.io/mbcav>
- Marone, C. (1998). Laboratory-derived friction laws and their application to seismic faulting. *Annual Review of Earth and Planetary Sciences*, 26(1), 643–696. <https://doi.org/10.1146/annurev.earth.26.1.643>
- McClure, M. W. (2015). Generation of large postinjection-induced seismic events by backflow from dead-end faults and fractures. *Geophysical Research Letters*, 42, 6647–6654. <https://doi.org/10.1002/2015GL065028>
- McClure, M. W., & Horne, R. N. (2010). *Discrete fracture modeling of hydraulic stimulation in enhanced geothermal systems*. Paper presented at the Proceedings of the 35th Workshop on Geothermal Reservoir Engineering.
- McClure, M. W., & Horne, R. N. (2011). Investigation of injection-induced seismicity using a coupled fluid flow and rate/state friction model. *Geophysics*, 76(6), WC181–WC198. <https://doi.org/10.1190/geo2011-0064.1>
- McGarr, A. (2014). Maximum magnitude earthquakes induced by fluid injection. *Journal of Geophysical Research: Solid Earth*, 119, 1008–1019. <https://doi.org/10.1002/2013JB010597>
- McNamara, D. E., Benz, H. M., Herrmann, R. B., Bergman, E. A., Earle, P., Holland, A., et al. (2015). Earthquake hypocenters and focal mechanisms in Central Oklahoma reveal a complex system of reactivated subsurface strike-slip faulting. *Geophysical Research Letters*, 42, 2742–2749. <https://doi.org/10.1002/2014GL062730>
- Megies, T., & Wassermann, J. (2014). Microseismicity observed at a non-pressure-stimulated geothermal power plant. *Geothermics*, 52, 36–49. <https://doi.org/10.1016/j.geothermics.2014.01.002>
- Norbeck, J. H., & Horne, R. N. (2016). Evidence for a transient hydromechanical and frictional faulting response during the 2011  $M_w$  5.6 Prague, Oklahoma earthquake sequence. *Journal of Geophysical Research: Solid Earth*, 121, 8688–8705. <https://doi.org/10.1002/2016JB013148>
- Pampillón, P., Santillán, D., Mosquera, J. C., & Cueto-Felgueroso, L. (2018). Dynamic and quasi-dynamic modeling of injection-induced earthquakes in Poroelastic media. *Journal of Geophysical Research: Solid Earth*, 123, 5730–5759. <https://doi.org/10.1029/2018JB015533>
- Passelègue, F. X., Brantut, N., & Mitchell, T. M. (2018). Fault reactivation by fluid injection: Controls from stress state and injection rate. *Geophysical Research Letters*, 45, 12,837–12,846. <https://doi.org/10.1029/2018GL080470>
- Rice, J. R. (1993). Spatio-temporal complexity of slip on a fault. *Journal of Geophysical Research*, 98(B6), 9885. <https://doi.org/10.1029/93JB00191>
- Rice, J. R., & Ben-Zion, Y. (1996). *Slip complexity in earthquake fault models*. Paper presented at the Earthquake prediction: The scientific challenge, Proc. Natl. Acad. Sci. USA, Irvine, CA (pp. 3811–3818).
- Rivet, D., De Barros, L., Guglielmi, Y., Cappa, F., Castilla, R., & Henry, P. (2016). Seismic velocity changes associated with aseismic deformations of a fault stimulated by fluid injection. *Geophysical Research Letters*, 43, 9563–9572. <https://doi.org/10.1002/2016GL070410>
- Rubino, V., Rosakis, A. J., & Lapusta, N. (2017). Understanding dynamic friction through spontaneously evolving laboratory earthquakes. *Nature Communications*, 8(1), 15991. <https://doi.org/10.1038/ncomms15991>
- Schmittbuhl, J., Lengliné, O., Cornet, F., Cuenot, N., & Genter, A. (2014). Induced seismicity in EGS reservoir: The creep route. *Geothermal Energy*, 2(1). <https://doi.org/10.1186/s40517-014-0014-0>
- Schoenball, M., & Ellsworth, W. L. (2017). A systematic assessment of the spatiotemporal evolution of fault activation through induced seismicity in Oklahoma and southern Kansas. *Journal of Geophysical Research: Solid Earth*, 122, 10,189–10,206. <https://doi.org/10.1002/2017JB014850>
- Schultz, R., Stern, V., Novakovic, M., Atkinson, G., & Gu, Y. J. (2015). Hydraulic fracturing and the crooked Lake sequences: Insights gleaned from regional seismic networks. *Geophysical Research Letters*, 42, 2750–2758. <https://doi.org/10.1002/2015GL063455>
- Segall, P. (1989). Earthquakes triggered by fluid extraction. *Geology*, 17(10), 942. [https://doi.org/10.1130/0091-7613\(1989\)017%3C0942:ETBFE%3E2.3.CO;2](https://doi.org/10.1130/0091-7613(1989)017%3C0942:ETBFE%3E2.3.CO;2)
- Segall, P., & Lu, S. (2015). Injection-induced seismicity: Poroelastic and earthquake nucleation effects. *Journal of Geophysical Research: Solid Earth*, 120, 5082–5103. <https://doi.org/10.1002/2015JB012060>

- Shapiro, S. A., Huenges, E., & Borm, G. (1997). Estimating the crust permeability from fluid-injection-induced seismic emission at the KTB site. *Geophysical Journal International*, *131*(2), F15–F18. <https://doi.org/10.1111/j.1365-246X.1997.tb01215.x>
- Shapiro, S. A., Krüger, O. S., Dinske, C., & Langenbruch, C. (2011). Magnitudes of induced earthquakes and geometric scales of fluid-stimulated rock volumes. *Geophysics*, *76*(6), WC55–WC63. <https://doi.org/10.1190/geo2010-0349.1>
- Shapiro, S. A., Rothert, E., Rath, V., & Rindschwentner, J. (2002). Characterization of fluid transport properties of reservoirs using induced microseismicity. *Geophysics*, *67*(1), 212–220. <https://doi.org/10.1190/1.1451597>
- Shirzaei, M., Ellsworth, W. L., Tiampo, K. F., Gonzalez, P. J., & Manga, M. (2016). Surface uplift and time-dependent seismic hazard due to fluid injection in eastern Texas. *Science*, *353*(6306), 1416–1419. <https://doi.org/10.1126/science.aag0262>
- Stark, M. A., & Davis, S. D. (1996). Remotely triggered microearthquakes at the geysers geothermal field, California. *Geophysical Research Letters*, *23*(9), 945–948. <https://doi.org/10.1029/96GL00011>
- Uenishi, K., & Rice, J. R. (2003). Universal nucleation length for slip-weakening rupture instability under nonuniform fault loading. *Journal of Geophysical Research*, *108*(B1), 2042. <https://doi.org/10.1029/2001JB001681>
- Urpi, L., Rinaldi, A. P., Rutqvist, J., Cappa, F., & Spiers, C. J. (2016). Dynamic simulation of CO<sub>2</sub>-injection-induced fault rupture with slip-rate dependent friction coefficient. *Geomechanics for Energy and the Environment*, *7*, 47–65. <https://doi.org/10.1016/j.gete.2016.04.003>
- van Thienen-Visser, K., & Breunese, J. N. (2015). Induced seismicity of the Groningen gas field: History and recent developments. *The Leading Edge*, *34*(6), 664–671. <https://doi.org/10.1190/tle34060664.1>
- Wei, S., Avouac, J.-P., Hudnut, K. W., Donnellan, A., Parker, J. W., Graves, R. W., et al. (2015). The 2012 Brawley swarm triggered by injection-induced aseismic slip. *Earth and Planetary Science Letters*, *422*, 115–125. <https://doi.org/10.1016/j.epsl.2015.03.054>
- Witherspoon, P. A., Wang, J. S. Y., Iwai, K., & Gale, J. E. (1980). Validity of cubic law for fluid flow in a deformable rock fracture. *Water Resources Research*, *16*(6), 1016–1024. <https://doi.org/10.1029/WR016i006p01016>
- Yeck, W. L., Hayes, G. P., McNamara, D. E., Rubinstein, J. L., Barnhart, W. D., Earle, P. S., & Benz, H. M. (2017). Oklahoma experiences largest earthquake during ongoing regional wastewater injection hazard mitigation efforts. *Geophysical Research Letters*, *44*, 711–717. <https://doi.org/10.1002/2016GL071685>
- Yeck, W. L., Weingarten, M., Benz, H. M., McNamara, D. E., Bergman, E. A., Herrmann, R. B., et al. (2016). Far-field pressurization likely caused one of the largest injection induced earthquakes by reactivating a large preexisting basement fault structure. *Geophysical Research Letters*, *43*, 10,198–10,207. <https://doi.org/10.1002/2016GL070861>
- Zhang, F., Damjanac, B., & Huang, H. (2013). Coupled discrete element modeling of fluid injection into dense granular media. *Journal of Geophysical Research: Solid Earth*, *118*, 2703–2722. <https://doi.org/10.1002/jgrb.50204>
- Zhang, F., Damjanac, B., & Maxwell, S. (2019). Investigating hydraulic fracturing complexity in naturally fractured rock masses using fully coupled multiscale numerical modeling. *Rock Mechanics and Rock Engineering*, *52*(12), 5137–5160. <https://doi.org/10.1007/s00603-019-01851-3>
- Ziv, A., & Rubin, A. M. (2003). Implications of rate-and-state friction for properties of aftershock sequence: Quasi-static inherently discrete simulations. *Journal of Geophysical Research*, *108*(B1), 2051. <https://doi.org/10.1029/2001JB001219>
- Zoback, M. D., Kohli, A., Das, I., & McClure, M. W. (2012). *The importance of slow slip on faults during hydraulic fracturing stimulation of shale gas reservoirs*. Paper presented at the SPE Americas Unconventional Resources Conference, Society of Petroleum Engineers, Pittsburgh, Pennsylvania, USA. <https://doi.org/10.2118/155476-MS>